Chemical Science

Accepted Manuscript

This article can be cited before page numbers have been issued, to do this please use: A. Martini, E. Borfecchia, K. A. Lomachenko, I. Pankin, C. Negri, G. Berlier, P. Beato, H. Falsig, S. Bordiga and C. Lamberti, *Chem. Sci.*, 2017, DOI: 10.1039/C7SC02266B.

ROYAL SOCIETY OF CHEMISTRY

rsc.li/chemical-science

ROYAL SOCIETY OF CHEMISTRY
View Article Online
DOI: 10.1039/C7SC02266B

Chemical Science

ARTICLE

Composition-driven Cu-speciation and reducibility in Cu-CHA zeolite catalysts: a multivariate XAS/FTIR approach to complexity

Received 00th January 20xx,
Accepted 00th January 20xx

DOI: 10.1039/x0xx00000x

www.rsc.org/

A. Martini[a], E. Borfecchia[a,b]*, K. A. Lomachenko[c,d], I. A. Pankin[a,d], C. Negri[a], G. Berlier[a], P. Beato[b], H. Falsig[b], S. Bordiga[a], C. Lamberti[d,e]

The small pore Cu-CHA zeolite is attracting increasing attention as a versatile platform to design novel single-site catalysts for deNO$_x$ applications and for the direct conversion of methane to methanol. Understanding at the atomic scale how the catalyst composition influences the Cu-species formed during thermal activation is a key step to unveil the relevant composition-activity relationships. Herein, we explore by *in situ* XAS the impact of the Cu-CHA catalyst composition on the temperature-dependent Cu-speciation and reducibility. Advanced multivariate analysis of *in situ* XANES in combination with DFT-assisted multi-component EXAFS fits and *in situ* FTIR spectroscopy of adsorbed N_2 allows us to obtain unprecedented quantitative structural information on the complex dynamics during the speciation of Cu-sites inside the framework of the CHA zeolite.

1 Introduction

Cu-exchanged chabazite (Cu-CHA) is currently the object of intensive research efforts to rationalize its outstanding performance in the NH_3-assisted selective catalytic reduction (SCR) of NO_x[1-3] and its recently proved low-temperature activity in the direct conversion of methane to methanol.[4-9] Among the multitude of zeolite topologies, CHA sticks out due to its structural simplicity. The framework is build up by an arrangement of double 6-member rings (*d6r*), connected via 4-member ring units, giving rise to the so-called *cha* cages, which are accessible through 8-member rings (*8r*). All the tetrahedral sites (T-sites) occupied by Si or Al atoms are in crystallographic equivalent positions.[10, 11] Such a structural simplicity fostered the investigation of Cu-CHA as a model system to resolve fundamental questions of structure-performance relationships in metal-exchanged zeolite catalysis.[12]

Initial structural studies proposed isolated Cu(I) or Cu(II) cations to exclusively occupy one extra-framework site in the plane of the 6-member rings (*6r*).[13-15] However, with the exponentially increasing number of studies in the recent years, it has become evident that the CHA topology offers multiple docking sites for cations, and that the chemical properties (oxidation state, coordination geometry, nuclearity) and location of Cu-species in Cu-CHA are strongly influenced by the sample composition in terms of Si/Al ratio and Cu-loading.[1, 16-18] Importantly, Cu-speciation in the catalyst appears to be a dynamic process and largely driven by the environmental conditions, such as temperature and gas feed composition. In the particular case of the presence of H_2O or NH_3, framework-interacting Cu species can easily convert into mobile complexes,[19-22] freely suspended in the zeolite cages while undergoing redox chemistry, as proposed in a recently published low-temperature SCR mechanism.[23] Advanced *in situ/operando* characterization approaches and appropriate analytic tools allowing to manage complex spectroscopic datasets are thus mandatory to properly address the fickle nature of the active metals sites as well as to catch the dynamic host-guest interactions in these fascinating materials.

We have previously combined *in situ*/*operando* X-ray absorption (XAS) and emission spectroscopy (XES) to shed light on the structural and electronic properties of Cu-species formed during thermal activation,[24] and during interaction with a complete SCR-feed[22] or individual SCR-feed components.[3, 19, 25] To limit the number of experimental variables, most of these studies were systematically conducted on a Cu-CHA catalyst with fixed composition (Cu/Al ~ 0.44; Si/Al ~ 13), providing optimal SCR performance. However, as mentioned above, Cu-

[a]*Department of Chemistry, NIS Centre and INSTM Reference Center, University of Turin, Via Giuria 7, Turin, 10125 Italy.*
[b]*Haldor Topsøe A/S, Haldor Topsøes Allé 1, Kgs. Lyngby, 2800 Denmark.*
[c]*European Synchrotron Radiation Facility, 71 avenue des Martyrs, CS 40220, Grenoble Cedex 9, 38043 France.*
[d]*IRC "Smart Materials", Southern Federal University, Zorge str. 5, Rostov-on-Don, 344090 Russia.*
[e]*Department of Chemistry, CrisDi Centre and INSTM Reference Center, University of Turin, Via Giuria 7, Turin, 10125 Italy.*

†Electronic Supplementary Information (ESI) available: samples description and synthesis details, experimental setup for in situ XAS and FTIR spectroscopy, details MCR-ALS method, details on DFT-assisted XANES simulations; details on the determination of N_{pure} by PCA; MCR-ALS results for downsized and upsized component spaces; additional information to support the assignment of theoretical XANES curves; details on EXAFS analysis; details on IR spectral deconvolution. See DOI: 10.1039/x0xx00000x

speciation in CHA is strongly affected by the catalyst composition (Cu/Al and Si/Al ratios), and in order to derive structure-activity relationships in catalytic processes, it is absolutely necessary to perform a systematic study on different catalyst compositions.

Recent studies[18, 21, 26, 27] indicate the presence of two major Cu-sites in activated Cu-CHA, with markedly different redox properties and relative abundance depending on composition. These include reduction-resistant $Z_2Cu(II)$ species hosted in the *6r* of the CHA framework (where Z_2 indicates coordination to framework oxygens O_{fw} in the proximity of two neighbouring charge-balancing Al in framework T-sites, i.e. *2Al*) and redox-active Z[Cu(II)OH] complexes (where Z denotes bonds to O_{fw} next to an isolated Al in a framework T-site, i.e. *1Al*) preferentially located in the *8r*[11] and identified as the dominant structural component in high-loading Cu-CHA with Si/Al ~ 13.[24, 28]

Aiming at a comprehensive experimental exploration of the composition effects on Cu-speciation in activated Cu-CHA, we synthesized a systematic series of Cu-CHA samples, with Si/Al and Cu/Al ratios in the ~ 5–29 and ~ 0.1–0.6 ranges, respectively. A detailed description of the synthesis procedures and of the compositional characterization of all catalysts is reported in ESI Sec. 1.1†. We explore by *in situ* XAS the composition-dependent Cu-speciation of such catalysts during thermal treatment in He flow from RT to 400 °C (He-activation), in order to differentiate between the different reducibility of Cu-sites and gain deeper insights into the so-called *self-reduction* process in Cu-zeolites.[29-32]

Indeed, even after decades of research, the formation of large Cu(I) populations during the thermal treatment of Cu-exchanged zeolites in *vacuum* or inert gas flow, thus in the absence of any manifest reducing agent, is still puzzling the scientific community.[30-32] The self-reduction process is now gathering renewed interest in the context of the direct methane to methanol conversion on Cu-zeolites, where a mechanism is envisaged that requires the reaction of Cu(I) sites with O_2 to form CH_4-activating Cu-oxo species.[32]

Multivariate curve reconstruction (MCR) analysis of temperature-dependent XANES in combination with multi-component EXAFS fits allowed us to single out the XAS signatures of individual Cu-species formed in the CHA cages and achieve unprecedented quantitative information on composition *versus* Cu-speciation relationships. The composition-dependent reducibility and the complex nature of the ZCu(I) species resulting from self-reduction of Z[Cu(II)OH] complexes are further investigated using FTIR spectroscopy of adsorbed N_2. XAS and FTIR results reported hereafter merge into a consistent picture, adding novel traits of complexity to the state-of-the-art understanding of composition- and conditions-driven Cu-speciation in Cu-CHA.

2 Results and discussion

View Article Online
DOI: 10.1039/C7SC02266B

2.1 *In situ* XAS during He-activation on Cu-CHA catalysts at different composition

As demonstrated by the recent literature on Cu-zeolite catalysts,[1, 2, 7, 21, 24, 33] *in situ* Cu K-edge XAS is an ideal technique to access direct information on the average electronic properties and coordination environment of the metal centres hosted in the zeolite cages.[34-37] In order to track the dynamic rearrangements of Cu ions as a function of the environmental parameters, we collected *in situ* XANES during He-activation from 25 °C to 400 °C (flow rate 100 ml/min; heating rate 5 °C/min; XANES scan duration ~ 6 min) for six Cu-CHA samples with Si/Al ratios of ~ 5, 15, 19, 29 and Cu/Al ratios from ~ 0.1 to ~ 0.6. Experimental details on the gas-flow setup and XAS acquisition parameters are reported in ESI Sec. 1.2†.

Figure 1a shows the evolution of *in situ* XANES of the investigated Cu-CHA catalysts during He-activation from 25 °C to 400 °C. The XANES features follow similar trends in the whole series of samples, in agreement with previous studies by us[19, 24] and others.[21] The spectroscopic features emerging during activation can be qualitatively interpreted on the basis of the abundant literature on Cu K-edge XANES in metal-exchanged zeolites[1-3, 7, 19, 22, 24, 25, 29, 30, 38-45] and Cu active sites in biologically-relevant systems.[46-48] In particular, a progressive decrease of the intense white-line peak at ~ 8996 eV, characteristic of mobile five/six-coordinated Cu aquo-complexes,[24, 49-52] is observed as activation proceeds, paralleled by the development of the rising-edge peaks in the 8985–8987 eV range, reflecting an increase in the population of four/three-coordinated Cu(II) sites.[29, 31, 47, 53] From ~ 230 °C upwards, the self-reduction occurs in all the samples, which can be tracked by the development of XANES features in 8981–8985 eV range typical of Cu(I) sites in non-linear, low-coordination-number environments.[29, 38, 42, 46, 54, 55]

We also collected higher-quality *in situ* XAS spectra on the whole sample series upon stabilization at 400 °C in He. The acquisition time was adjusted to achieve a satisfactory S/N ratio in the EXAFS region (the corresponding k-space $k^2\chi(k)$ EXAFS spectra are reported in the ESI, Sec. 5.1†), enabling quantitative fitting of the resulting EXAFS spectra, see ESI Sec. 1.2.2† for details. Figure 1b-d compares the final states reached in He flow at 400 °C for all samples, in both XANES (Figure 1b) and EXAFS region (Figure 1c,d). A progressive modulation of the XAS features as a function of the composition can be appreciated. The rising-edge and post-edge peaks in the XANES occur at very similar positions in the whole sample series, although their relative intensity is different depending on composition. The reducibility (relative abundance of Cu(I) species at 400 °C) of the samples seems to be mostly determined, in a non-monotonous way, by the Si/Al ratio. Lower reducibility is observed for both Si/Al = 5 and Si/Al =19, 29 samples, although the dominant dehydrated Cu(II) species appear to be different in the two cases. In particular, the XANES for He-activated Cu-CHA at Si/Al = 5 shows a more intense and structured white line region, with well-resolved peaks at ~ 8998 and ~ 8992 eV, and a broad post-edge peak in the 9005–9010 eV range (blue asterisks in Figure

View Article Online
DOI: 10.1039/C7SC02265B

1b), in agreement with the XAS spectra reported by Paolucci *et al.*[21] for a Cu-CHA catalyst with similar composition (Cu/Al = 0.08; Si/Al = 5). Conversely, the samples with Si/Al = 19, 29 show broader and less pronounced white-line peaks, as well as a smoother post-edge region. The catalysts with intermediate Al content, Si/Al = 14, 15, are characterized by very pronounced Cu(I) XANES features, pointing out the presence of a majority of Cu(I) sites at 400 °C in He, irrespectively of Cu-loading.

The reducibility trends qualitatively identified throughout the series of samples are also supported by the modulations in the intensity of the weak pre-edge peak at ca. 8977 eV, mostly deriving from the 1s→3d transition, which unambiguously fingerprints the presence of d^9 Cu(II) ions in the catalysts[38, 46, 47, 56] (see Figure 1b, inset). Such peak is clearly visible for all the investigated samples except for the Si/Al ~ 14, 15 ones, where it appears almost completely smeared at both high (Cu/Al = 0.5) and low (Cu/Al = 0.1) Cu-loading.

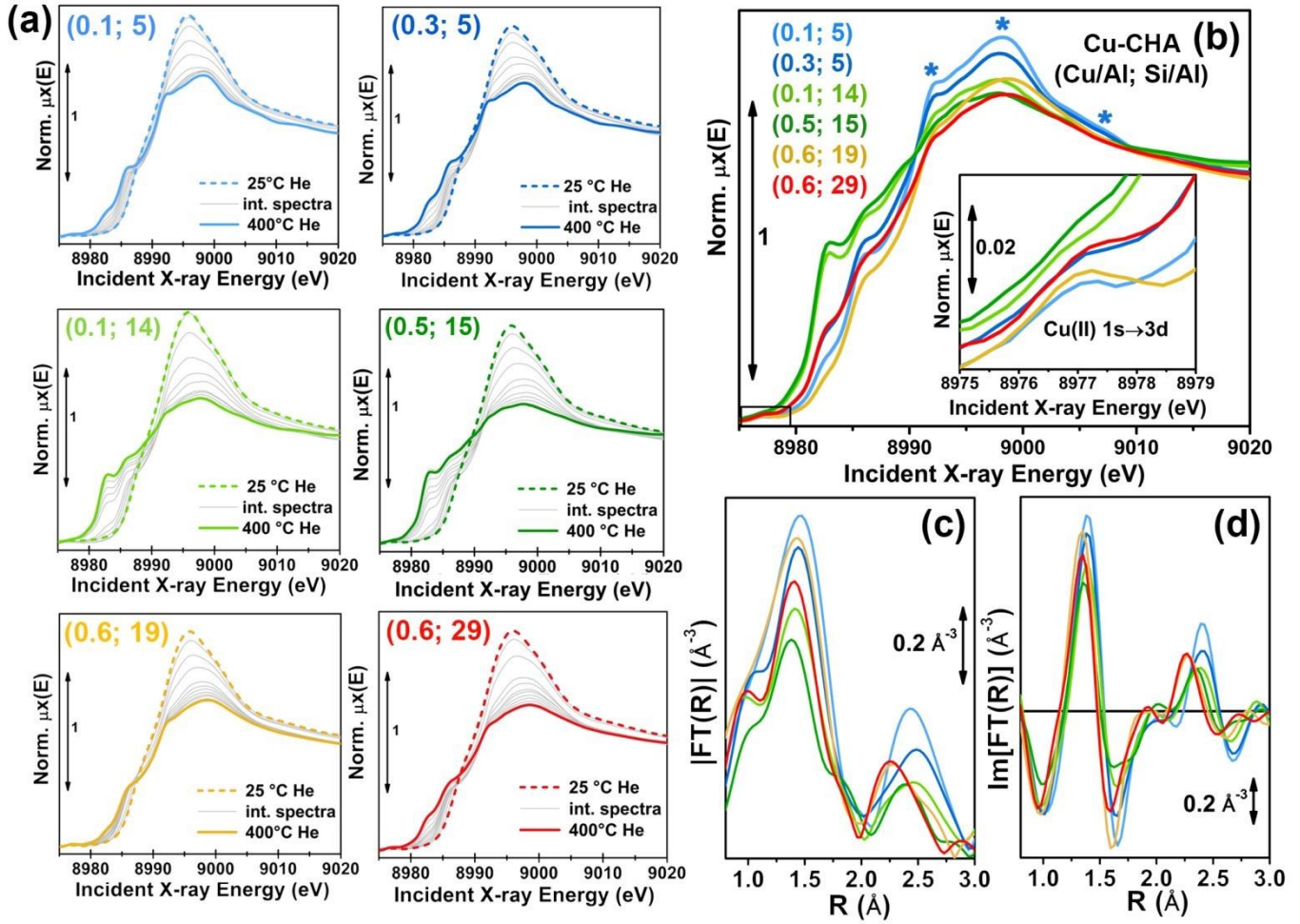

Figure 1. (a) *In situ* XANES of Cu-CHA catalysts with different composition (different samples are denoted with (Cu/Al; Si/Al) labels) during dehydration in He flow from 25 °C to 400 °C, heating rate 5 °C/min. (b) Comparison between XANES spectra of He-activated Cu-CHA samples with different composition, collected at 400 °C. The inset reports a magnification of the weak pre-edge peak mostly deriving from the dipole-forbidden 1s→ 3d transition in Cu(II) sites. (c, d) Magnitude (c) and imaginary parts (d) of the k^2-weighted, phase uncorrected, Fourier transformed EXAFS spectra (k-range 2.4-12.4 Å^{-1}) of He-activated Cu-CHA samples with different composition, collected at 400 °C. Colour code in all the panels: dashed thick lines: hydrated sample at 25 °C; solid thick lines: dehydrated sample at 400 °C; grey thin lines: intermediate spectra.

For all the He-activated samples, two well defined maxima are distinguishable in the phase-uncorrected FT-EXAFS spectra (Figure 1c,d), occurring in the 1.4–1.5 Å and 2.2–2.4 Å ranges. Based on the DFT-assisted EXAFS analysis previously performed on a Cu-CHA sample with Cu/Al ~ 0.44, Si/Al ~ 13,[24] we can safely assign the first maximum to single scattering (SS) paths involving extra-framework (O_{ef}) and framework (O_{fw}) O atoms in framework-coordinated Cu-species. Remarkably, the composition-induced modulation in the first-shell intensity correlates with the reducibility as evaluated from XANES. Indeed, samples with Si/Al = 5 and Si/Al = 19, 29 show higher first-shell intensities, suggesting a major population of Cu(II) sites characterized by three/four-fold coordination to O ligands. Conversely, a lower first-shell intensity is observed at Si/Al 14, 15, corresponding to a higher relative fraction of two-fold coordinated Cu(I) sites.

Based on several recent XAS studies on Cu-CHA,[3, 21, 22, 24, 43] we assign the principal contribution in the second maximum of the FT-EXAFS spectra to SS paths involving second-shell Al/Si T-atoms of the zeolite framework (T_{fw}). Notably, this

View Article Online
DOI: 10.1039/C7SC02266B

characteristic EXAFS feature has been previously employed to discriminate between framework-interacting Cu-sites and ammonia-solvated mobile Cu-complexes in *operando* NH_3-SCR studies on Cu-CHA.[3, 21, 22] We observe a clear composition-driven trend in both intensity and position (evident looking at the imaginary part of the FT-EXAFS spectra in Figure 1d) of the second-shell EXAFS peak. As the Si/Al ratio increases from 5 to 29, the peak progressively shifts towards lower R-values, evidencing an average shortening in Cu−T_{fw} bond distances (see also Section 2.4 for quantitative analysis). The intensity of the second-shell peak is mostly determined by the Si/Al ratio; a minimum is found in correspondence of the Si/Al = 14, 15 samples, according to the following trend: Si/Al = 5 > 19, 29 > 14, 15.

Interestingly, the highest reducibility at Si/Al ~ 15 is accompanied by damped and broadened second shell peaks, possibly connected with a higher heterogeneity in Cu(I) siting (see below, Sections 2.4 and 2.5). The higher second-shell intensity observed for Si/Al = 5 is in good agreement with the presence of a major contribution from *2Al* Z_2-Cu(II) sites. For these Cu-sites, DFT-optimized geometries previously reported in the literature,[11, 21, 24, 28] evidence two almost degenerated Cu−Al and Cu−Si SS paths at ~ 2.8 Å contributing to the second maximum in the FT-EXAFS (please note that Si and Al atomic neighbours are not distinguishable by EXAFS due to the very similar scattering amplitude). Conversely, for the case of *1Al* Z[Cu(II)OH] sites, only one Al neighbour at ~ 2.7 Å is predicted, which would result in a lower second-shell peak in the FT-EXAFS spectra.

The qualitative observations presented so far will be rationalized in the following, by combining multivariate analysis of the temperature-dependent XANES dataset shown in Figure 1a and multi-component fitting of the EXAFS spectra reported in Figure 1c,d.

2.2 Multivariate analysis of temperature-dependent *in situ* XANES

As highlighted in the previous section, qualitative analysis of the *in situ* XAS dataset during He-activation reported in Figure 1 strongly supports the presence of a common set of Cu-species, occurring with different relative abundance as a function of the temperature *T* and composition (*Cu/Al*; *Si/Al*). Thus, normalized experimental XANES spectra at each temperature and composition, μ^{exp} (*Cu/Al*; *Si/Al*, *T, E*), can be described as linear combinations (LC) of a limited number N_{pure} of reference XANES spectra of pure Cu-species/sites, μ_i^{pure} (*E*), with composition- and temperature-dependent weights w_i^{pure} (*Cu/Al*; *Si/Al*, *T*), according to eq. (1):

$$\mu^{exp}\left(\frac{Cu}{Al};\frac{Si}{Al},T,E\right) = \sum_{i=1}^{N_{pure}} w_i^{pure}\left(\frac{Cu}{Al};\frac{Si}{Al},T\right)\cdot\mu_i^{pure}(E) \qquad \text{eq. (1)}$$

XANES linear combination fit (LCF) analysis has been established as a powerful tool for disentangling the different contributions in complex multi-component spectral series, and successfully applied to rationalize Cu-speciation during *in situ/operando* experiments on Cu-based catalysts.[22, 33, 40, 57] Nonetheless, a bottleneck in the effective application of this method is the availability of a proper set of reference spectra.

It is now well known that under certain conditions, e.g. for the as-prepared pre-catalyst at RT in air or during low-temperature SCR,[18, 20, 21] the Cu cations in Cu-CHA are efficiently solvated by H_2O or NH_3, yielding mobile aquo or amino complexes scarcely interacting with the zeolite framework. In such conditions, molecular complexes in solution can be readily used as references in LCF analysis, yielding excellent results in the determination of Cu-speciation.[21] However, when framework-interacting Cu-species are formed, the selection of a suitable set of references is not straightforward, due to the unusual coordination configurations. Intriguingly, these resemble the low-coordination/low symmetry environments of the active sites in metallo-proteins,[47, 57, 58] and are difficult to replicate synthetically. With this respect, we have attempted to reproduce the XANES spectra of the He-activated Cu-CHA samples reported in Figure 1b by using conventional LCF analysis with a series of relevant experimental references, namely hydrated Cu(II), $[Cu(II)(NH_3)_4]^{2+}$, CuO and Cu_2O. However, LCF resulted in an unsatisfactory reproduction level of the experimental data, with R-factor values in the 0.05-0.1 range, depending on catalyst composition. Computational analysis has played a key role in identifying major Cu-species in dehydrated Cu-CHA, but despite the enormous progress in DFT-assisted XANES simulations,[32, 33, 59-62] in most of the cases the line-to-line agreement between experimental and theoretical spectra, required to directly employ theoretical references for XANES LCF analysis, is still difficult to achieve.

To address this challenge, we explored a novel route in the analysis of the multi-composition temperature-dependent dataset reported in Figure 1, exploiting multivariate curve resolution (MCR) techniques[58-60] to deduce XANES spectra of pure Cu-species directly from the available experimental data. These chemometric methods are helpful in resolving mixtures, once the number of pure constituents N_{pure} is independently determined, by estimating their response profiles and their concentrations (in our case normalized XANES spectra μ_i^{pure} (*E*) and composition- and temperature-dependent weights w_i^{pure} (*Cu/Al*; *Si/Al*, *T*), see eq. (1) and ESI Sec. 1.4†). The proliferation of *operando* XAS spectroscopy, involving the time-efficient collection of big datasets during dynamic process-relevant conditions, is triggering an increasing demand for automated data analysis strategies. In this context, MCR methods, originally developed and widely employed by the analytical chemistry community, have recently emerged as versatile tools in the rationalization of time-resolved *in situ/operando* spectroscopic data in heterogeneous catalysis, and a few examples of application to XAS studies can be found in the literature.[61-65]

Notably, once a series of μ_i^{pure} (*E*) spectra is extracted by MCR-ALS, DFT-assisted XANES simulations represent a powerful tool to qualitatively guide *a posteriori* the assignment of each component to specific metal environments (see below).

The first step in our analysis involved the determination of N_{pure} in the multi-composition temperature-dependent XANES dataset in Figure 1a. To this aim, we performed principal

View Article Online
DOI: 10.1039/C7SC02266B

component analysis (PCA) of the *in situ* XANES series (He-activation from 25 to 400 °C) for each catalyst composition.

PCA has been performed assuming that any systematic thermal dependence of the XANES signal is negligible with respect to the Cu-speciation-related contributions to the experimental variance (see ESI Sec. 2.1† for details and justification of this hypothesis). From inspection of the Scree plots and quantitative analysis using Malinowski F-test (5% significance level) and IND-factor,[58] we identified an average number of pure species $\langle N_{pure} \rangle = 5 \pm 1$ (see also ESI Sec. 2†). Subsequently, we employed an MCR approach, based on the alternating least square (ALS) method[59, 60] to extract chemically meaningful spectra and concentration profiles of pure Cu-species/sites during the He-activation process. MCR-ALS analysis was performed using the GUI (Graphical User Interface) developed by Tauler and co-workers,[66] see ESI Sec. 1.4† for details.

Being aware that the selection of N_{pure} could significantly influence the MCR-ALS results, we systematically repeated the analysis for N_{pure} values in the 3–6 range. The reconstruction results obtained upsizing/downsizing the component space around $N_{pure} = 5$ are reported in ESI Sec. 3†. These were carefully assessed in terms of (i) convergence of the MCR-ALS algorithm, (ii) ability to reproduce all the characteristic XANES features (local maxima in the theoretical $\mu_i^{pure}(E)$ curves) identified in the experimental dataset, (iii) trends in the R-factor values for the reconstruction, (iv) presence of overlapping contributions in the derived concentration profiles, (v) chemical and spectroscopic meaningfulness of the derived scenarios. All these indicators strongly support that the number of pure components identified by statistical analysis, $N_{pure} = 5$, represents an optimal value within the available data quality and time-resolution, as also confirmed by the low R-factor values and residuals obtained for the adopted five-component model (see below, Section 2.3 and ESI Sec. 1.4.2, 3.2†).

Figure 2 summarizes the results from MCR-ALS analysis of He-activation in Cu-CHA as a function of temperature and catalyst composition. The five theoretical XANES spectra of pure components $\mu_i^{pure}(E)$ are shown in Figure 2a while the bar plots in Figure 2b report their correspondent temperature-dependent concentration profiles for each compositional point. By matching the characteristic XANES features of each $\mu_i^{pure}(E)$ spectrum and the evolution trends for their weights w_i^{pure} (*Cu/Al*, *Si/Al*; *T*) with the rich experimental background currently available on Cu-CHA, we were able to safely assign each pure component to the Cu-species depicted in Figure 2c, as we will discuss hereafter. Further support to the assignment will be derived from comparison with the experimental Cu K-edge XANES spectra of selected reference compounds and by DFT-assisted XANES simulations based on the models reported in Figure 2c.

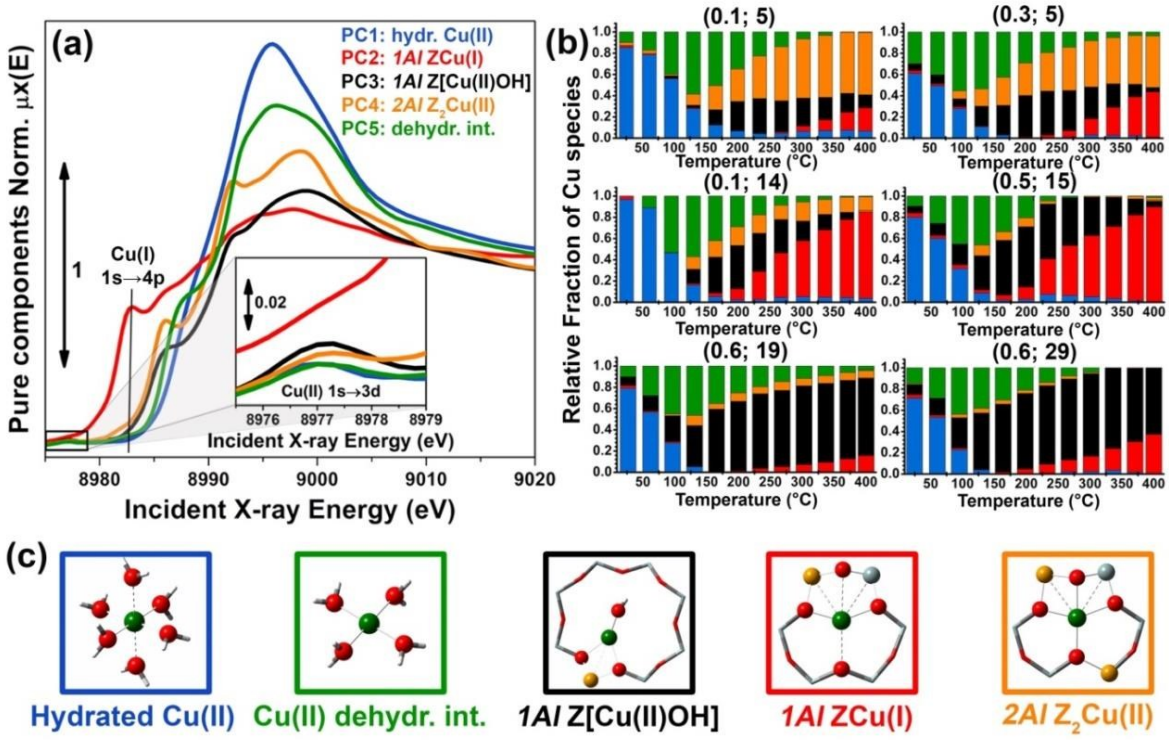

Figure 2. Results of MCR-ALS analysis of global temperature-dependent XANES dataset collected on six Cu-CHA samples with different composition during He-activation from 25 to 400 °C (Figure 1a), assuming $N_{pure} = 5$. (a) XANES spectra of pure components $\mu_i^{pure}(E)$ derived from MCR-ALS. The inset reports a magnification of the Cu(II) 1s → 3d transition region in the theoretical spectra. (b) Temperature-dependent abundance of pure species, w_i^{pure} (*Cu/Al*; *Si/Al*, *T*), in each of the catalysts (bars have the same colours as the corresponding spectra in panel (a). (c) Proposed assignment of the five pure components to specific Cu-species/sites formed in the Cu-CHA catalyst as a function of composition and activation temperature, using the same colour code as in parts (a,b). Blue (PC1): mobile Cu(II)-aquo-complexes $[Cu(II)(H_2O)_n]^{2+}/[Cu(II)(H_2O)_{n-1}(OH)]^+$ with n = 6; green (PC5): Cu(II) dehydration intermediate, possibly represented by mobile $[Cu(II)(H_2O)_n]^{2+}/[Cu(II)(H_2O)_{n-1}(OH)]^+$ complexes with n = 4; black (PC3): *1Al* Z[Cu(II)OH] sites in their oxidized form; red (PC2): *1Al* ZCu(I) sites in their reduced form, resulting from self-reduction of *1Al* Z[Cu(II)OH] species; orange (PC4): *2Al* Z_2Cu(II) sites. Atom colour code: Cu: green; H: white; O: red; Si: grey; Al: yellow.

View Article Online
DOI: 10.1039/C7SC02266B

Chemical Science

ARTICLE

A first clue to identify the Cu oxidation state in each of the retrieved pure components is provided by the 1s → 3d pre-edge peak in the theoretical pure spectra μ_i^{pure} (*E*) (see Figure 2a, inset). The peak is clearly present in all the μ_i^{pure} (*E*) curves except in the μ_2^{pure} (*E*) XANES for the PC2 component (red line in Figure 2a). Hence, this latter component can be unambiguously assigned to a d^{10} Cu(I) species, whereas the other four components correspond to Cu(II) moieties.

Considering the characteristic shape of the XANES spectrum, the PC1 component is easily assigned to mobile Cu(II)-aquo-complexes, namely $[Cu(II)(H_2O)_n]^{2+}$ or $[Cu(II)(H_2O)_{n-1}(OH^-)]^+$ with n = 6. For all the probed compositions, these fully hydrated Cu(II) ions represent the dominant component at the beginning of the activation process, and their concentration drops rapidly to values < 10% total Cu as temperature reaches ~ 150 °C. Further support to such assignment and, in general, to the spectroscopic reliability of the theoretical XANES derived by MCR-ALS, is provided by the comparison between the μ_1^{pure} (*E*) curve and the reference XANES for an aqueous solution of Cu(II) acetate, see ESI Sec. 4.1†.

The decrease in the relative fraction of fully hydrated Cu(II) is paralleled by the transient growth in the contribution of a different component (PC5), whose concentration peaks in the 100−130 °C range for all the samples. The correspondent μ_5^{pure} (*E*) spectrum is characterized by a lower intensity and a broader shape in the XANES white-line region. A shoulder becomes evident in the edge-rising region at ~ 8987 eV. We tentatively assign such component to a four coordinated, pseudo square-planar Cu(II) 'dehydration intermediate', based on the similarity of the corresponding MCR-ALS XANES to the spectra of reference four-coordinated Cu(II) species, i.e. Cu(II)O and $[Cu(II)(NH_3)_4]^{2+}$ (see ESI Sec. 4.1†). Mobile Cu(II) complexes such as $[Cu(II)(H_2O)_4]^{2+}$/$[Cu(II)(H_2O)_3(OH)]^+$ or alternatively, four-coordinated Cu(II) moieties with mixed O_{fw}/O_{ef} ligation could be envisaged. Remarkably, the contribution from this species is appreciable until 250−280 °C (albeit with longer tails in the Si/Al = 19, 29 samples), which matches well the temperature threshold at which no more adsorbed molecular water was observed by FTIR on a Cu-CHA catalyst with Si/Al ~ 13; Cu/Al ~ 0.44.[24]

The decay in the population of the dehydration intermediate described above paves the way to the actual birth of fully dehydrated framework-interacting Cu-species. It is here that the impact of the catalyst composition on temperature-dependent Cu-speciation comes strikingly into play. Two Cu(II) species start to form almost simultaneously after ~ 130 °C, namely the PC3 and PC4 components, that we assign to *1Al* Z[Cu(II)OH] and *2Al* Z_2Cu(II) sites, respectively. Such an assignment is supported by several evidences. Firstly, the PC4 component dominates the high-temperature Cu-speciation at Si/Al = 5, reaching at 400 °C relative fractions from ~ 40 to ~ 60% of total Cu depending on the loading. Conversely, it always represents a minor component (< 20% total Cu) at both intermediate (Si/Al = 14, 15) and low (Si/Al= 19, 29) Al content. Moreover, after 250 °C, the contribution from PC4 is substantially stable,[§] whereas the PC3 population is progressively eroded in favour of PC2, the only Cu(I) component extracted by MCR-ALS. Spectroscopically, the correspondent $\mu_{3,4}^{pure}$ (*E*) spectra properly reflect the differences observed in the experimental data as a function of the composition. In particular, the μ_4^{pure} (*E*) curve associated to *2Al* Z_2Cu(II) sites optimally reproduces both the higher, highly structured, white line peak and the post-edge peak observed in the experimental XANES of He-activated samples at Si/Al = 5.

Finally, the PC2 contribution is straightforwardly attributed to *1Al* ZCu(I) sites, resulting from self-reduction of *1Al* Z[Cu(II)OH] species. The correspondent μ_2^{pure} (*E*) spectrum shows all the characteristic fingerprints of two-coordinated non-linear Cu(I) sites,[24, 29, 38, 42, 46, 54, 55] with a prominent rising-edge peaks developing from ~ 8982 eV and a lower white line intensity with respect to the other Cu-species identified so far.

As anticipated, to further support these assignments we have simulated the Cu K-edge XANES spectra for all the five model structures reported in Figure 2c and proposed to interpret the MCR-ALS μ_i^{pure} (*E*) spectra; computational details on the strategy adopted to calculate the theoretical XANES for each DFT-model can be found in ESI Sec. 1.5†. The five simulated XANES spectra and the correspondent μ_i^{pure} (*E*) curves from MCR-ALS analysis are compared in Figure 3.

Focusing on the three framework-interacting Cu-species which dominate Cu-speciation in the He-activated catalysts, we observe how the simulated XANES curves properly reproduce the distinctive relative energy shifts (and partially, intensity ratios) of the rising-edge peaks for each Cu-site. The ZCu(I) model, in agreement with our assignment to PC2, results in prominent peaks significantly red-shifted and more intense with respect to the Z[Cu(II)OH] and Z_2Cu(II) geometries. In line with the assignment to PC4, the Z_2Cu(II) site gives rise to a sharp peak at ~ 8986 eV, to two well defined maxima in the white-line region at ~ 8992 eV and ~ 8998 eV, and a broad post-edge peak around 9007 eV. The alternative Cu(II) environment, Z[Cu(II)OH], is associated to a broader rising-edge peak and less defined features in the white line region, globally shifted to higher energy, in qualitative agreement with the PC3 curve.

View Article Online
DOI: 10.1039/C7SC02266B

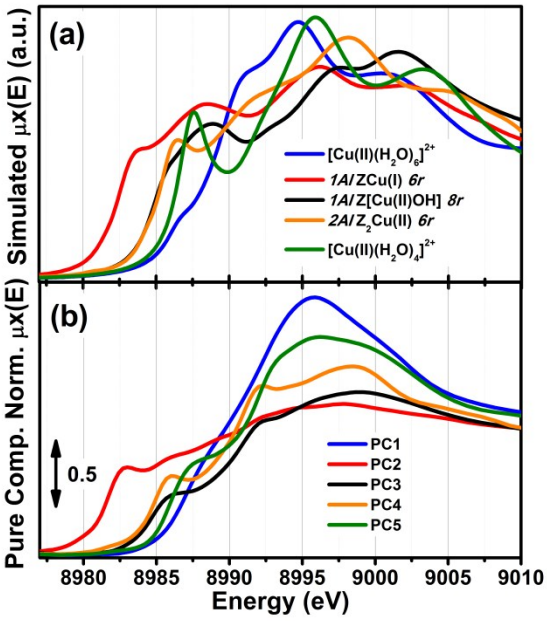

Figure 3. (a) Simulated Cu K-edge XANES spectra for the five DFT-optimized model structures reported in Figure 2c and proposed to interpret the MCR-ALS μ_i^{pure} (E) spectra. (b) μ_i^{pure} (*E*) spectra obtained from MCR-ALS analysis for comparison.

Theoretical spectra for fully- and under-coordinated Cu(II) aquo-complexes are clearly distinguished from the ones of framework-interacting Cu-species due to the presence of high-intensity transitions in the 8990-8998 eV range, as observed in the MCR-ALS spectra for PC1 and PC5. Interestingly, the simulations evidence how, while decreasing the number of H_2O ligands in the first Cu(II) coordination sphere from six to four, a well-defined rising-edge peak develops at ~ 8987 eV. The same behaviour is recognized while comparing μ_1^{pure} (*E*) and μ_5^{pure} (*E*) curves, together with a slight blue-shift of the white-line peak for PC5, which is also reproduced in the simulated spectra for $[Cu(II)(H_2O)_4]^{2+}$ and $[Cu(II)(H_2O)_6]^{2+}$. Beside the simulations reported in Figure 3, we have also considered an intermediate $[Cu(II)(H_2O)_5]^{2+}$ model, aiming to improve the reproduction of the PC5 species. As it can be observed in ESI Sec. 4.2†, $[Cu(II)(H_2O)_4]^{2+}$ and $[Cu(II)(H_2O)_5]^{2+}$ substantially give rise to an equivalent set of peaks, but their relative intensity and energy position (especially in the white-line region) are affected by the number of H_2O ligands. Although the similarity with four-coordinated reference compounds (see Figure S10b) suggests predominant ligation to 4 H_2O ligands, simulations indicate that the μ_5^{pure} (*E*) spectrum could actually evidence a dynamic mix of four-, five-, and, possibly, even lower-coordinated Cu(II) aquo complexes, which are however not readily resolvable within time- and energy-resolution of the available dataset. To resolve the additional complexity associated with the transition between mobile and framework-interacting Cu-species, we envisage additional studies employing molecular dynamics-assisted XANES simulations[67, 68] in combination with High Energy Resolution Fluorescence Detected (HERFD) XANES measurements, ensuring both higher energy resolution and improved time-resolution to accurately sample the 130-200 °C temperature range where the highest concentration of PC5 is observed.

2.3 Interpretation of the MCR-ALS results: novel elements of complexity affecting reducibility in Cu-CHA

From the MCR-ALS analysis discussed above, several insights into the impact of the catalyst composition on Cu-speciation during He-activation can be derived. At RT, Cu-speciation is largely dominated by mobile, fully-coordinated Cu aquo-complexes (always > 60% total Cu). Nonetheless, small populations of partially dehydrated Cu(II) species together with traces (< 5% total Cu) of framework-interacting Cu(II) and Cu(I) sites are already found at the beginning of the activation process. The birth of fully dehydrated Cu-sites occurs in all samples through the transient development of a common Cu(II) 'dehydration intermediate', as described before. As shown in Figure 2b, Cu-speciation for all the He-activated catalysts at 400 °C can be described as a combination of redox-active *1Al* sites (in their oxidized Z[Cu(II)OH] or reduced ZCu(I) form) and redox-inert *2Al* $Z_2Cu(II)$ sites, in agreement with the picture proposed in the recent report by Paolucci et al.,[21] and with the two reduction peaks observed for Cu-CHA during H_2-TPR at ~ 230 and 380 °C.[18, 26] Noteworthy, the different redox properties of *1Al* and *2Al* sites greatly favour their discrimination during thermal treatment in inert atmosphere, since Cu(I) and Cu(II) XANES features are much more readily discernible with respect to those of Cu(II) sites with slightly different coordination geometries.

Nonetheless, our analysis reveals novel elements of complexity, which will be addressed in more details in the following. To this aim, Figure 4 details the MCR-ALS results for the most representative compositional points, comparing experimental μ^{exp} (*Cu/Al; Si/Al, T, E*) and reconstructed μ^{rec} (*Cu/Al; Si/Al, T, E*) XANES at key temperatures during the He-activation (left panels) and reporting concentration profiles (right panels) for the five pure Cu-species identified by statistical analysis and assigned as described in Section 2.2. Reconstruction residuals for the selected temperatures and temperature-dependent R-factor values are also reported, demonstrating that the MCR-ALS procedure ensures an excellent reproduction of the experimental XANES dataset for all the investigated samples (almost 100 spectra).

The highest deviations (peaks in R-factor vs temperature profiles, which however is always well below 2%) are generally observed at the maximum population of the Cu(II) dehydration intermediate or nearby, when different dehydrated Cu(II) sites starts to develop. As already discussed at the end of Section 2.2 and suggested by the MCR-ALS results for N_{pure} = 6 (see ESI Sec. 3†), the transition from mobile aquo complexes to framework-interacting species could occur *via* additional intermediate states (possibly composition-specific), which however are not resolvable within our experimental time-resolution and cannot be reliably singled out by MCR-ALS.

Paolucci *et al.* computed a Cu-site compositional phase diagram for activated Cu-CHA, predicting the relative fraction of *1Al* and *2Al* sites as a function of Si/Al and Cu/Al ratios.[21] Such a diagram represents a milestone in Cu-CHA research. However, it involves

View Article Online
DOI: 10.1039/C7SC02266B

some assumptions. In particular, it is derived assuming that *2Al* $Z_2Cu(II)$ sites in the *6r* represent the first framework sites to be populated by the cations during dehydration.

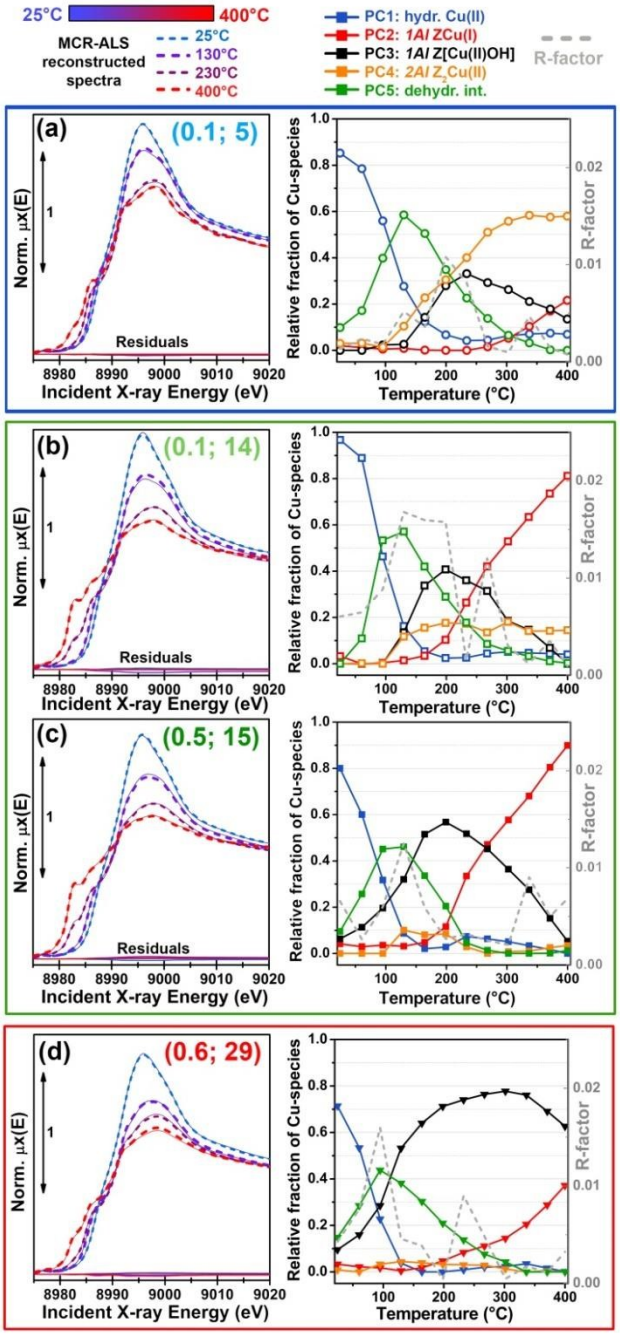

Figure 4. Detailed MCR-ALS results for the most representative compositional points: (a) Cu/Al = 0.1, Si/Al = 5; (b) Cu/Al = 0.1, Si/Al = 14; (c) Cu/Al = 0.5, Si/Al = 15; (d) Cu/Al = 0.6, Si/Al = 29. Left panels: comparison between experimental *in situ* XANES μ^{exp} during He-activation (thin solid lines) and reconstructed spectra μ^{rec} from MCR-ALS at the four key temperatures of 25 °C, 125 °C, 230 °C, 400 °C with the corresponding residuals. Right panels: concentration profiles for the five pure Cu-species/sites identified in our model as a function of the activation temperature (coloured symbols) and correspondent R-factor values (grey dashed lines).

Under this hypothesis, only after all the available *2Al* sites at a given Si/Al ratio are saturated, Cu is allowed to populate other kind of sites, primarily forming *1Al* Z[Cu(II)OH] complexes in the *8r*. Similar assumptions were previously adopted by Bates *et al.*[69] to compute the Cu/Al ratio required to saturate the available *6r 2Al* sites as a function of the Si/Al ratio in the parent zeolite. According to this model, catalysts with Cu-loadings below the saturation threshold would contain after dehydration only *2Al* $Z_2Cu(II)$ sites: for Si/Al = 5, 15 and 29, saturation is predicted at Cu/Al ≈ 0.24, 0.09, and 0.05 respectively.

However, the results reported in Figure 4 reveal a more complex picture in relation with the population of *2Al* $Z_2Cu(II)$ sites, particularly evident at intermediate Si/Al values. We note that for all the investigated samples, *2Al* $Z_2Cu(II)$ and *1Al* Z[Cu(II)OH] sites (orange and black symbols in Figure 4, respectively) start to form almost simultaneously during dehydration, which deviates from an ideal *2Al* saturation scenario. Comparing the MCR-ALS results for the Si/Al = 5 catalysts with lower (Cu/Al = 0.1) and higher (Cu/Al = 0.3) loading, a saturation tendency is confirmed: due to the finite availability of *6r*s hosting *2Al* sites, at higher Cu-loading a lower relative fraction of $Z_2Cu(II)$ species is observed, counterbalanced by a larger population of reducible *1Al* sites. Nevertheless, for the catalyst with Cu/Al = 0.1, Si/Al = 14 (Figure 4b), the final state at 400 °C is characterized by a substantial fraction of reduced ZCu(I) sites (~ 80%), whereas the $Z_2Cu(II)$ contribution reaches a maximum abundance of only ~ 18%. Assuming saturation of *2Al* sites, this sample should be dominated by redox-inert *2Al* sites due to its low Cu-loading (> 90% total Cu according to the compositional phase diagram in ref.[21] and the saturation threshold evaluated by Bates *et al.*[69]). Experimentally, this is however clearly not the case: MCR-ALS evidences only a relatively small increase in the abundance of *2Al* sites with respect to the high-loading catalyst with comparable Si/Al ratio (Cu/Al = 0.5; Si/Al = 15, Figure 4c). This effect could be connected with high barriers for Cu migration towards *2Al* sites, possibly trapping the cations into local energy minima at *1Al* sites.

Another intriguing result emerging from MCR-ALS analysis is that the reducibility level for *1Al* sites is clearly dependent on Al distribution, with highest reducibility for Si/Al ~ 15 (< 10% Cu observed as *1Al* Z[Cu(II)OH] at 400 °C) and lower reducibility at Si/Al = 19 and 29, with ~ 70% and ~ 60% of the *1Al* sites still surviving in the oxidized form, respectively (see Figure 2b and Figure 4d). These results unambiguously demonstrate that self-reduction proceeds though a cooperative multi-step process involving proximal acid sites, the availability of which is ultimately determined by Al density and distribution in the zeolite. This is in line with previously suggested mechanisms in the literature.[21, 30-32] Plausibly, the process initiates with the thermally-driven reduction of Z[Cu(II)OH] to ZCu(I), accompanied by the release of an hydroxyl radical, OH·.[30-32] The availability/spatial proximity of a reactive channel for the OH· radical might then determine the overall efficiency of the self-reduction process, and the final balance between *1Al* sites in oxidized/reduced form observed in the He-activated catalysts. Consequently, Al-rich frameworks facilitate self-reduction. Nevertheless, in Cu-CHA (and, we might speculate, in general for *d6r* zeolites) the same condition also promotes large populations of redox-inert $Z_2Cu(II)$ sites hosted in *6r*, lowering the average reducibility of the catalysts, and blurring the overall

DOI: 10.1039/C7SC02266B

picture. With respect to the Cu-loading impact on reducibility, when comparing concentration profiles for ZCu(I) on low- (Cu/Al ~ 0.1) and high- (Cu/Al ~ 0.5) loading Cu-CHA at almost equivalent Si/Al of ~ 15, we observe very similar temperature onsets and rates for the self-reduction (see Figure 4b,c). A slightly lower Cu(I) fraction is observed at 400 °C in the low-loading sample, but it excellently correlates with the small increase in the concentration of $Z_2Cu(II)$ sites. Hence, at optimal Si/Al values, Cu-loading seems to poorly affect the self-reduction efficiency, which can be conjecturally connected with a role of proximal Brønsted sites along parallel/alterative pathways efficiently affording ZCu(I) species. Within the time-resolution (~ 6 min) of our XANES experiments, intermediate Cu(II) species eventually formed along the transformation from Z[Cu(II)OH] to ZCu(I) are not detected. From a structural point of view, it is however important to underline that the initial $[Cu(II)OH]^+$ complexes and other putative mono- and multimeric intermediates proposed in the literature (e.g. $[Cu(II)O]^+$[30, 31] and mono-(μ-oxo) dicopper[7, 32, 70]) all retain a very similar tridentate coordination geometry for the Cu(II) centres, expected to result in very similar XANES signatures. Hence, even assuming that such tridentate Cu(II)-moieties do form and have macroscopic lifetime in the catalyst before undergoing reduction to Cu(I) *via* extra-framework oxygen desorption,[71, 72] they could be easily assimilated in the same structural component as Z[Cu(II)OH] in MCR-ALS analysis. $[Cu(II)OH]^+$ and $[Cu(II)O]^+$ complexes would be also virtually indistinguishable by EXAFS, due to the low scattering amplitude of H. Conversely, the formation of significant fractions of dicopper cores, possibly as a result of self-organization phenomena,[73] should be traceable in the FT-EXAFS spectra *via* high-amplitude metal-metal contributions.

Finally, we note that for most of the samples, MCR-ALS analysis evidences a non-monotonous trend in the concentration profiles of hydrated Cu(II)-species (PC1 in Figure 4), showing a small peak in the high-temperature range (230-350 °C) which account for up to 5% total Cu increments in the relative fractions of fully hydrated Cu(II). Due to the reduced entity of the variations and the absolute weakness of the contribution from this structural component in the high-temperature range, it is difficult to conclusively establish the physico-chemical meaningfulness of the effect. However, it is interesting to note that the temperature position of the peak correlates with the initial rise in the ZCu(I) component, supporting that the initial steps in the pathway(s) to self-reduction involve the formation of small amounts of H_2O. These traces of water could transiently re-solvate and mobilize a small fraction of Cu sites: for samples (Cu/Al = 0.5; Si/Al = 15) and (Cu/Al = 0.6; Si/Al = 29), the increase in relative fractions of hydrated Cu(II) apparently occurs to the expenses of *2Al* $Z_2Cu(II)$ sites (see Figure 4c,d).

2.4 Structural analysis of *1Al* and *2Al* Cu-sites by multi-component EXAFS fits

Aiming at a further validation of the composition-speciation relationships discussed above and at a deeper structural characterization of the local coordination environment of the Cu ions hosted at *1Al* and *2Al* sites, we performed quantitative analysis of the *in situ* EXAFS spectra collected at 400 °C after dehydration in He (experimental data reported in Figure 1c,d). Here, singling out the contributions from the different Cu-sites is not straightforward. Unconstrained multi-component fits would result in an excess of strongly correlated free parameters, definitely yielding not reliable results. To obtain a robust set of constrains, we carried out a preliminary fitting step by selecting the compositional points characterized by the purest Cu-speciation at 400 °C (see also ESI Sec. 5†), showing dominant contributions from each of the framework-interacting Cu-species evidenced by MCR-ALS, i.e. *1Al* sites in their oxidized Z[Cu(II)OH] or reduced ZCu(I) form and *2Al* $Z_2Cu(II)$ sites.

Importantly, at this stage, we also examined alternative environments for ZCu(I) and $Z_2Cu(II)$, based on the DFT models obtained in our previous study,[24] and already employed for the XANES simulations reported in Figure 3. ZCu(I), initially formed from reduction of Z[Cu(II)OH] moieties in the *8r*, could either remain in *8r* plane, or migrate to the energetically-favoured site in the *6r*.[11, 13] The two locations are associated to different Cu local environments (especially in the second coordination sphere, see Table S5, ESI Sec. 5.2†), which might result in rather similar XANES signatures[24] but different EXAFS features in the 2−3 Å range. Here, EXAFS analysis identifies the *6r* site as the most likely configuration, but also evidences an increased structural disorder accompanying the self-reduction process. Indeed, both models resulted in a lower fit quality and higher Debye-Waller (DW) factors with respect to the cases where the Cu(II) oxidation state is largely dominant, either in the form of *1Al* Z[Cu(II)OH] or *2Al* $Z_2Cu(II)$ species. Notably, Göltl *et al.*[74] have recently modelled by *ab initio* molecular dynamics simulations the movements of bare Cu(I) and Cu(II) cations in Cu-CHA at 300 K. The authors highlight how, already at RT, the local coordination of the Cu cations changes significantly, with larger movements for Cu(I), predicted to be more weakly bound to the framework with respect to Cu(II). The possible compresence of a favoured docking site in *6r* with a secondary contribution from *1Al* ZCu(I) sites in *8r*, together with the enhanced mobility of Cu(I) at 400 °C is in excellent agreement with the blurring effect emerging for our EXAFS analysis. The co-existence of two different sites for Cu(I) in *6r* and *8r* was also pointed out in a very recent quasi-simultaneous PXRD/XANES study.[75] Further insights on this point will be provided by *in situ* FTIR of adsorbed N_2, as discussed in Section 2.5.

View Article Online
DOI: 10.1039/C7SC02266B

Chemical Science

ARTICLE

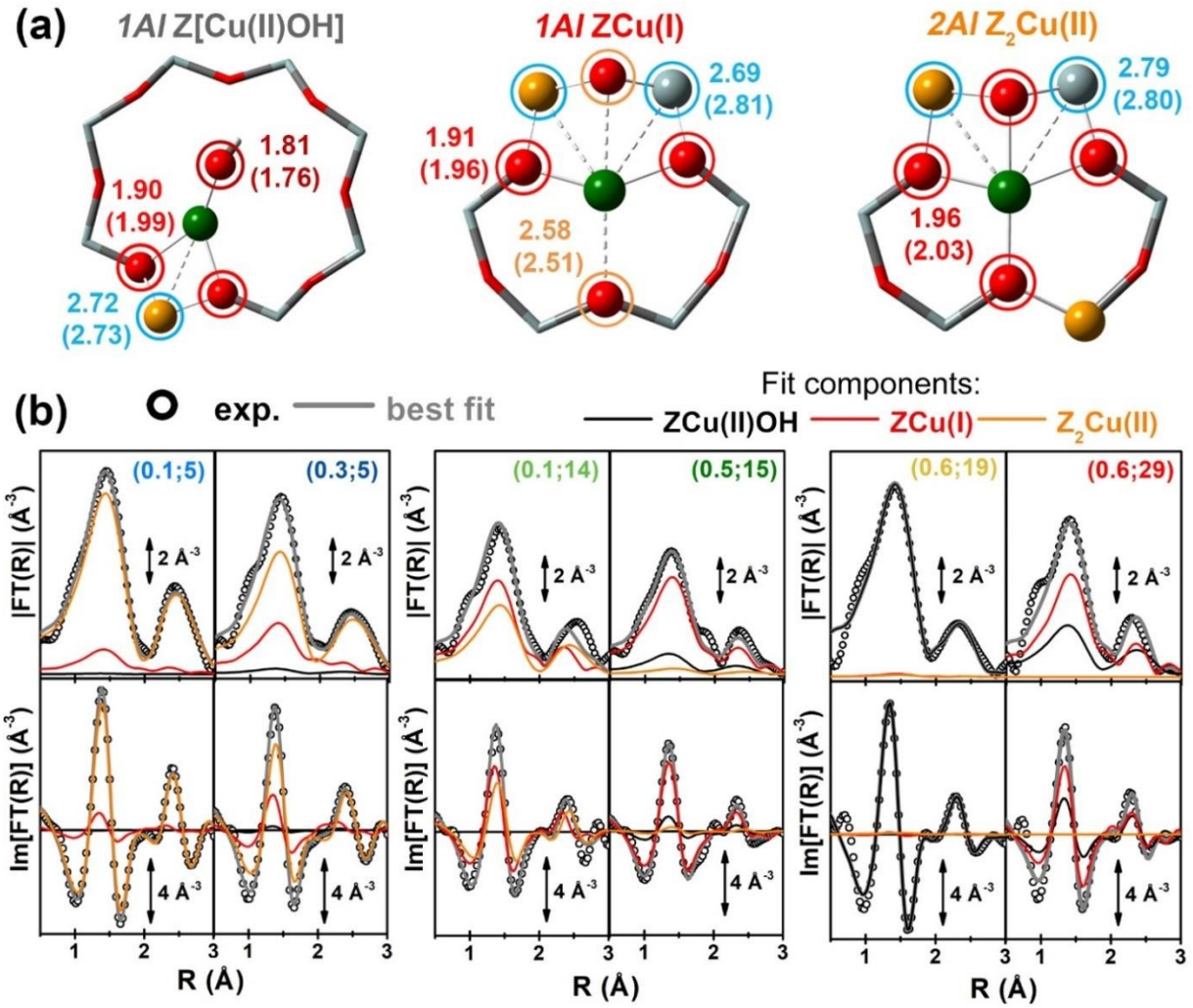

Figure 5. (a) DFT-optimized structural models for framework-interacting Cu-species dominating Cu-speciation in He-activated Cu-CHA at 400 °C, namely *1Al* Z[Cu(II)(OH)], *1Al* ZCu(I), and *2Al* Z_2Cu(II) sites. The atoms located the first and second coordination shell of Cu are shown in ball-and-stick mode (atom colour code: Cu, green; H, white; O, red; Si, grey; Al, yellow) and highlighted with coloured circles indicating the different coordination shells included in the EXAFS fitting model (Cu–O_{ef}: wine; Cu–O_{fw}: red; Cu–O'_{fw}: orange; Cu–T_{fw}: blue). For each shell, the average bond distances from Cu refined by mono-component EXAFS fits are reported in Å, whereas the correspondent starting values from DFT are reported in parentheses. (b) Comparison between experimental (black circles) and best fit (light grey thick lines) FT-EXAFS spectra (top panel: magnitude, bottom panels: imaginary part) obtained from multi-component fits on the whole Cu-CHA sample series; for each sample, the weighted contributions from the three dehydrated Cu-species included in the fitting model are also reported as thin solid lines (*1Al* Z[Cu(II)OH]: grey, *1Al* ZCu(I): red; *2Al* Z_2Cu(II): orange). The correspondent experimental and best fit $k^2\chi(k)$ curves in k-space can be found in the ESI, Sec. 5.5†. In part (b), sample composition is indicated by (Cu/Al; Si/Al labels).

View Article Online
DOI: 10.1039/C7SC02266B

Table 1. Results from multi-component EXAFS fits of He-activated state at 400 °C for the whole multi-composition sample series. Fits performed in the k-range (2.4–11.0) Å^{-1} and R-range (1.0–3.2) Å. For all the fits, geometries of *1Al* Z[Cu(II)OH], *1Al* ZCu(I), and *2Al* Z2Cu(II) Cu-species (i.e. radial shift parameters ΔR_i) have been fixed based on the results on mono-component fits on 'purest' He-activated states (*1Al* Z[Cu(II)OH] model for sample (0.6; 19), *1Al* ZCu(I) in *6r* for sample (0.5; 15), *2Al* $Z_2Cu(II)$ in *6r* with Al-Si-Si-Al linkage for sample (0.1; 5); see ESI Sec. 5.2†), and S_0^2 have been set to unity.

Composition (Cu/Al; Si/Al)	(0.1; 5)	(0.3; 5)	(0.1; 14)	(0.5; 15)	(0.6; 19)	(0.6; 29)
Fit R-factor	0.007	0.007	0.044	0.017	0.006	0.014
N_{par} (N_{ind})	8 (12)	8 (12)	8 (12)	8 (12)	8 (12)	8 (12)
ΔE (eV)	−5.8 ± 0.6	−6.0 ± 0.5	−7 ± 1	−7.0 ± 0.8	−3.2 ± 0.4	−3.8 ± 0.4
$A_{Z[Cu(II)OH]}$	0.0 ± 0.2	0.0 ± 0.1	0.0 ± 0.3	0.1 ± 0.2	1.0 ± 0.2	0.4 ± 0.1
$A_{ZCu(I)}$	0.2 ± 0.1	0.4 ± 0.1	0.7 ± 0.1	0.8 ± 0.2	0.0 ± 0.1	0.6 ± 0.2
$A_{Z2Cu(II)}$	0.8 ± 0.2	0.6 ± 0.1	0.3 ± 0.1	0.1 ± 0.1	0.0 ± 0.1	0.0 ± 0.1
$\sigma^2_{O(ef)}$ (Å^2)	0.007±0.002	0.008±0.002	0.008±0.002	0.007±0.002	0.007±0.001	0.007±0.001
$\sigma^2_{O(fw)}$ (Å^2)	0.007±0.001	0.007±0.001	0.008±0.001	0.009±0.001	0.004±0.001	0.007±0.001
$\sigma^2_{T(fw)}$ (Å^2)	0.011±0.002	0.014±0.003	0.010±0.002	0.012±0.002	0.014±0.003	0.009±0.001

With respect to *2Al* $Z_2Cu(II)$ *6r* sites, within the limits imposed by the Löwenstein's rule,[76] two possible configurations exist, depending on the siting for the two charge-balancing Al atoms within the *6r*. In particular, –Al–Si–Al– and –Al–Si–Si–Al– linkages result in different Cu(II) local environments: in the latter case, Cu is shifted towards the centre of the *6r*, adopting a less distorted four-fold coordination to O_{fw}. EXAFS analysis indicates that this –Al–Si–Si–Al– configuration optimally describes the *2Al* $Z_2Cu(II)$ site, yielding a significantly lower fit R-factor with respect to the –Al–Si–Al– geometry (see Table S6, ESI Sec. 5.2†). This result provides experimental support to recent DFT calculations predicting a more efficient stabilization of bare Cu(II) sites in *6r* with –Al–Si–Si–Al– linkages.[12]

Mono-component EXAFS fits provided us with experimentally-optimized geometries for the three framework-interacting Cu-species expected to dominate Cu-speciation in He-activated Cu-CHA (see Figure 5a), setting the scene for a multi-component fitting protocol extended to the whole series of catalysts. To this aim, we calculated three sets of EXAFS paths including all the SS paths contributing in the 1.0 – 3.2 Å range for the Cu-sites shown in Figure 5a. For each geometry, we fixed bond distances to the best-fit values obtained in the correspondent mono-component fit, and set a global S_0^2 to the ideal value of 1. Hence, for each catalyst composition, we fitted DW factors for the relevant shell of atomic neighbours, and, most importantly, relative fractions A_i for each component, i = Z[Cu(II)OH], ZCu(I), $Z_2Cu(II)$. The results of multi-component EXAFS fits are summarized in Figure 5b and Table 1. For all catalysts, we were able to achieve a very good level of reproduction of the experimental EXAFS spectra by combining the three structural components singled out by MCR-ALS. The DW values refined for the different sub-shells of atomic neighbours are consistent with what found in previous studies, falling in the typical expectation ranges for high-temperature data collection on complex, multi-component systems.

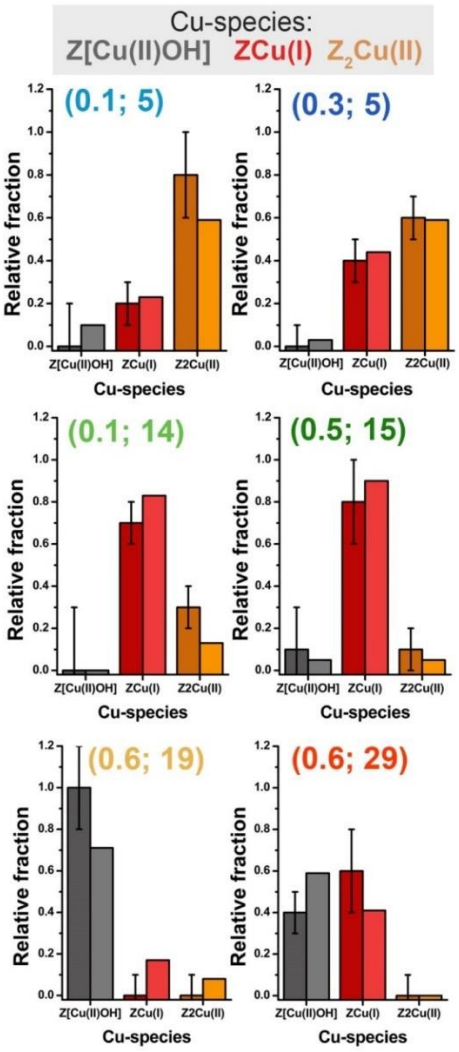

Figure 6. Relative fractions of framework-interacting Cu-species formed in He-activated Cu-CHA as a function of the catalyst composition (Z[Cu(II)OH]: grey; ZCu(I): red; $Z_2Cu(II)$: orange), evaluated from multi-component EXAFS fits (darker colours with error bars) and by MCR-ALS analysis of *in situ* XANES (lighter colours). Sample composition is indicated using (Cu/Al; Si/Al) labels.

View Article Online
DOI: 10.1039/C7SC02266B

The highest levels of structural disorder are still seen for Si/Al = 14, 15 samples. This is not surprising, due to the fickle nature of the Cu(I) component which dominates in these highly-reducible catalysts. For all the other samples, R-factor values well below 2% are obtained, in line with the lower mobility of Cu(II) ions.

Noteworthy, for all the investigated samples, the second-shell peak in the FT-EXAFS spectra is properly reproduced solely considering Cu–T_{fw} contributions, in excellent agreement with the different environments predicted for *1Al* and *2Al* sites shown in Figure 5a. In general, the multi-component fits reported in Figure 5b discourage a significant contribution of Cu–Cu paths in the second-shell region, i.e. in the 2.0–2.8 Å range of the phase-uncorrected FT-EXAFS. We cannot however exclude that such Cu–Cu scattering contributions could emerge at higher distances, where unfortunately the technique is not accurate enough. Further experiments, focusing on high-temperature activation in O_2 and employing enhanced data collection statistics to improve the S/N ratio in the high k-range would be needed to achieve conclusive results on the presence of diluted multimeric Cu-oxo moieties.

In the view of a cross-validation of the employed methods, Figure 6 compares, as a function of the catalyst composition, the relative fractions of Z[Cu(II)OH], ZCu(I), and Z_2Cu(II) species in He-activated Cu-CHA at 400 °C evaluated from MCR-ALS XANES analysis and multi-component EXAFS fits. Within the EXAFS fitting errors, the two methods yield a substantially comparable Cu-speciation in the final He-activated state, corroborating the speciation-composition trends discussed above.

2.5 Reducibility trends and Cu(I) siting from *in situ* FTIR of adsorbed N_2

In situ FTIR spectroscopy was employed as complementary technique to corroborate the reducibility trend of Cu sites observed by XAS in the same set of Cu-CHA samples. More in detail, herein we discuss the spectra obtained by using N_2 as a probe molecule, on vacuum-activated samples. Spectra were normalized with respect to pellet thickness and Cu content, as detailed in ESI Sec. 1.3†. N_2 is a weakly interacting probe, enabling discrimination between similar adsorption sites due to the very low perturbation induced on the involved cations.[77-79] Moreover, it selectively forms adducts (stable at liquid nitrogen temperature, ~ − 160 °C) with Cu(I) sites, [38, 80] and it is widely accepted that *vacuum* activation is equivalent to the treatment in inert flow (such as He), with respect to self-reduction.[19, 31] This means that the results described hereafter can be compared on a semi-quantitative ground to those discussed above for XAS.

N_2 adsorption on a *vacuum* activated Cu-CHA sample with Cu/Al ~ 0.44 and Si/Al ~ 13 was reported by Giordanino *et al.*, and compared to the results obtained on Cu-beta and Cu-ZSM-5 with similar composition.[80] The spectra are in perfect agreement to those of the (Cu/Al = 0.5; Si/Al = 15) Cu-CHA sample studied in this work, clearly showing two components: a predominant band at ~ 2292 cm^{-1} (light grey vertical line in Figure 7a) with a shoulder centred at ~ 2300 cm^{-1} (grey vertical line in Figure 7a). This implies the presence of two significantly different Cu(I) sites, in terms of cation local environment, in line with the report by Dědeček *et al.* who observed two distinct emission bands - assigned to Cu(I) ions in *8r* and *6r* - on a set of natural and synthetic Cu-CHA zeolites.[81]

Interestingly, the relative intensity of the two N_2 IR components changes in the set of samples, indicating a dependence of Cu(I) sites distribution on composition. In particular, in the spectra obtained on sample with Si/Al = 5 (first panel in Figure 7a) the high frequency component (HF) around 2300 cm^{-1} seems dominant with respect to the low frequency one (~ 2292 cm^{-1}, LF). An opposite trend is observed on the sample with Si/Al = 29 (right hand panel), while the samples with Si/Al = 14, 15 (middle panels) clearly show both components with relative intensity depending on Cu/Al ratios. Spectral deconvolution was carried out on the high coverage bands reported in Figure 7a (red curves), to semi-quantitatively estimate the abundance of the two Cu(I) sites. The procedure was first optimized for sample (Cu/Al = 0.1; Si/Al = 14), where the two components are more clearly defined. The resulting two best fits were then used as starting point to analyse the other samples, keeping fixed peaks width and/or shape (see ESI Sec. 6† for details). The average values of the normalized integrated areas calculated for each component are reported in the bar plot of Figure 7b, while Table 2 also shows the corresponding average position and width. The bar plot in Figure 7b also reports the total peaks area, which will be discussed in the following.

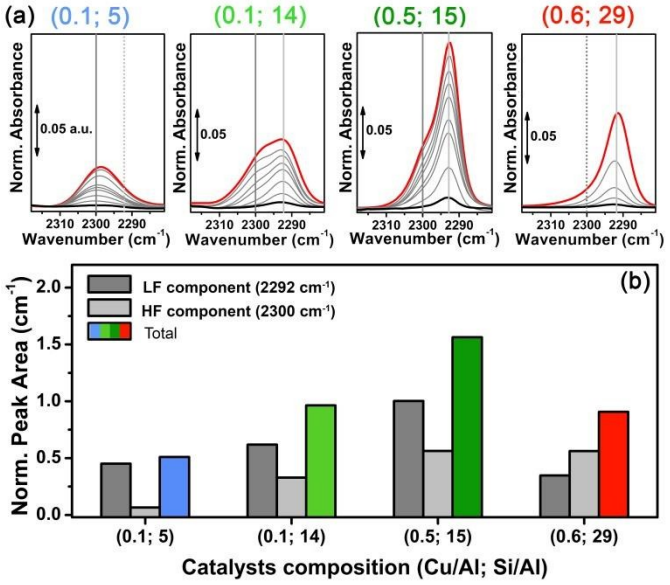

Figure 7. (a) Low temperature (~ − 160 °C) normalized FTIR spectra of N_2 dosed ad increasing equilibrium pressure (from 10^{-2} to 5 Torr) on vacuum-activated Cu-CHA catalysts with different composition, indicated by (Cu/Al; Si/Al) labels. Black, red and light grey curves refer to lowest, highest and intermediate N_2 coverage, respectively. (b) Normalized areas of the N_2/Cu(I) IR peaks measured at the highest coverage, including normalized areas of LF and HF components calculated by spectral deconvolution.

View Article Online
DOI: 10.1039/C7SC02362B

Table 2. Average position, width and normalized integrated area of the two N_2/Cu(I) IR components (high frequency, HF and low frequency, LF) calculated by spectral deconvolution, including assignment.

Composition (Cu/Al; Si/Al)	(0.1; 5)	(0.1; 14)	(0.5; 15)	(0.6; 29)
HF ~ 2300 cm^{-1} ZCu(I) *6r*				
Position (cm^{-1})	2299.0 ± 0.2	2299.0 ± 0.8	2296.0 ± 0.1	2297.0 ± 1
Width (cm^{-1})	11.2 ± 0.2	11.9 ± 0.9	12.0 ± 0.2	12 ± 2
Norm. Area (cm^{-1})	0.45	0.62	1.00	0.35
LF ~ 2292 cm^{-1} ZCu(I) *8r*				
Position (cm^{-1})	2291 ± 1	2291.0 ± 0.3	2292.00 ± 0.01	2291.0 ± 0.2
Width (cm^{-1})	11 ± 3	7.9 ± 0.6	5.1 ± 0.1	6.7 ± 0.4
Norm. Area (cm^{-1})	0.06	0.33	0.56	0.56

Concerning the quantitative estimations summarized in Figure 7b and Table 2, which confirms the dependence of the two components concentration upon composition, some considerations have to be made. First, the extinction coefficients of the HF and LF bands can be different, since they depend on the specific interaction of the dinitrogen ligand with the Cu(I) sites. As discussed elsewhere,[78, 80] the formation of Cu(I)·N_2 adducts involves both σ-donating and π-accepting interactions through the Cu(I) available *d* orbitals and the dinitrogen filled $3\sigma_g$ and empty $1\pi_g$ molecular orbitals, respectively. These interactions weaken the N≡N bond, resulting in the observed redshift with respect to the (Raman active) gas-phase value of 2321 cm^{-1}. Thus, a higher value for the redshift indicates a more effective σ-donation/d-back-donation interaction, which can be associated to a larger available space and/or a more effective cation ionic character.[78] On these bases, we can assign the LF component at ~ 2292 cm^{-1} to ZCu(I) sites in *8r*, and the HF one at ~ 2300 cm^{-1} to ZCu(I) sites in the *6r*, characterized by a more crowded coordinative environment, including two first-shell O_{fw} ligands at ca. 1.9 Å and two additional O'_{fw} atomic neighbours at ca. 2.6 Å (see DTF optimized structures in ESI, Table S5†).

As pointed out in Section 2.4, these two ZCu(I) sites are expected to have very similar XANES signatures, and their possible co-existence can account for the increased structural disorder observed in correspondence to large ZCu(I) populations. These observations are in very good agreement with the FTIR results, since the sites are distinguishable only by using the weak N_2 probe, while this is not the case with the CO probe (only one single band is observed in relation to Cu(I) CO adducts at 2155 cm^{-1} on Cu/Al ~ 0.44 and Si/Al ~ 13 Cu-CHA[80], and on the other samples studied in this work).

Unfortunately, to the best of our knowledge nothing can be said on the extinction coefficient of the two corresponding bands. For N_2 adducts formed with alkali-metal ions, mainly characterized by an electrostatic interaction, the intensity of the IR vibration was found to be a function of the electric field, and thus proportional to the observed blue shift.[82] Since the formation of Cu(I)·N_2 adducts is driven by σ-donation/d-back-donation interactions, no direct relations between the observed redshift and the corresponding extinction coefficients can be drawn. On the other hand, the average peak width values reported in Table 2 show that the HF component is distinctly broader with respect to the LF one. The only exception is sample with Si/Al = 5, where both the components are found with equivalent peak width of ca. 11 cm^{-1}. In this sample, however, the LF component represents a very minor contribution poorly defined in the deconvolution, as also evidenced by the higher error associated to its width. Such a peak broadening further supports the assignment of the HF component to ZCu(I) in *6r*, where the N_2 adduct could be perturbed by interactions with the framework in the small space of the *6r* window. This broadening, however, could induce an overestimation of the relative amount of this site, based on the integrated peak areas (bar plot of Figure 7b).

As mentioned above, Dědeček *et al.* showed a dependency on the intensity of the two Cu(I) luminescence bands on Cu loading.[81] According to the authors, *8r* should be populated first (low Cu-loading) and reach saturation at Cu/Al ~ 0.3, while *6r* are supposed to be populated only from Cu/Al = 0.1–0.2 and not saturate at higher Cu/Al ratios (~ 0.35). Unfortunately, the Si/Al ratio of the Cu-CHA zeolites studied by photoluminescence was not precisely stated, so that we cannot directly compare our results to those reported by Dědeček *et al*. However, these observations are in fair agreement with the estimated distribution of HF and LF Cu(I) sites on the two samples with Si/Al =14, 15 at low and high Cu loading (middle bars in Figure 7b).

Finally, and more importantly in this context, the integrated area of the N_2 peaks reported in Figure 7a (highest coverage, red curves) is compared in Figure 7b as coloured bars. These data (which are normalized with respect to Cu loading) can give an estimation about the Cu reducibility in the set of samples, similarly to what discussed on the basis of XAS data. This estimation is limited by the following considerations: (i) the integrated area is not strictly proportional to the Cu(I) content, since the N_2 adducts with the two possible ZCu(I) sites are likely to be characterized by different extinction coefficients, as discussed above; (ii) measurements were carried out at low temperature, while the XAS data was obtained *in situ* on the He-activated state at 400 °C; (iii) the efficiency of the self-reduction could be influenced by the activation conditions (*vacuum vs* inert flow). Notwithstanding these limitations, the observed trend in reducibility among the set of samples is in good agreement with XAS conclusions. Namely, reducibility increase passing from Si/Al = 5 to 15, where it reaches a maximum and then decreases at Si/Al = 29. Notice that, on the basis of what discussed above about the broadening of the HF component, self-reducibility could be slightly overestimated in samples with relatively high amount of the ZCu(I) *6r* site, thus justifying the small discrepancies of these results with XAS ones.

View Article Online DOI: 10.1039/C7SC02266B

3 Conclusions

In this work, we have employed *in situ* XAS to monitor the He-activation process in a multi-composition platform of Cu-CHA zeolites, aiming to clarify the influence of the catalyst composition on the temperature-dependent Cu-speciation and reducibility. The abundance of redox-active Cu species is indeed expected to profoundly impact the performance of Cu-CHA as catalysts in two of the currently most intensively studied processes over zeolite-based catalysis: NH_3-SCR and direct methane to methanol conversion, both known to involve redox chemistry at the metal centres. After principal component analysis of the temperature-dependent multi-composition XANES dataset, we employed a multi-variate curve resolution method to extract chemically-meaningful spectra and concentration profiles of pure components formed during He-activation as a function of the catalyst composition. Based on the spectroscopic fingerprints of each theoretical XANES and the correspondent temperature-dependent concentration profiles, we were able to reliably assign the theoretical spectra to pure Cu-species/sites. The assignment was subsequently corroborated by simulating the Cu K-edge XANES spectra for the correspondent model geometries. For the first time, this approach allowed us to rationalize in a quantitative frame the complex dynamics of Cu-cations in the CHA cages during the activation process. Noteworthy, it will now be possible to use the theoretical XANES generated by MCR-ALS as references in the quantitative determination of Cu-speciation in Cu-CHA samples with arbitrary composition and/or treated in different conditions by simple linear combination analysis.

In summary, the formation of framework-interacting Cu-species from the mobile Cu(II) aquo-complexes present at RT occurs, irrespectively of catalyst composition, via a Cu(II) dehydration intermediate, peaking around 130 °C. Then, *1Al* Z[Cu(II)OH] and *2Al* Z_2Cu(II) species develop almost simultaneously, with relative abundances strongly influenced by Si/Al ratio in the parent zeolite. *1Al* Z[Cu(II)OH] species, dominant for samples with Si/Al = 15-29, peak around 200 °C and then progressively decrease at elevated temperatures, in favour of reduced *1Al* ZCu(I) species. Conversely, *2Al* Z_2Cu(II) sites, dominant at Si/Al = 5, reach a steady population in the 200–300 °C range and remain stable until 400 °C. Cu-speciation at 400 °C can be described for all samples as a combination of redox-active *1Al* sites, in their oxidized and reduced form, and redox-inert *2Al* Z_2Cu(II) sites.

By quantitatively monitoring the composition-driven Cu-speciation during He-activation of Cu-CHA, we highlighted novel traits of complexity accompanying the transition from mobile Cu-complexes to framework-interacting Cu-species and the subsequent self-reduction process. In particular, the high reducibility observed in the low-loading sample (Cu/Al = 0.1) with Si/Al = 14 and the almost simultaneous development of *1Al* and *2Al* populations both contrast with an ideal *2Al* sites saturation scenario, often assumed in the current literature. Moreover, the reducibility level of *1Al* sites is shown to depend on Si/Al (optimal reducibility for Si/Al = 15, lower reducibility at Si/Al = 19, 29), evidencing that self-reduction proceeds though a cooperative multi-step process involving proximal acid sites, whose availability is ultimately determined by Al density and distribution in the zeolite.

The MCR-ALS XANES results are also combined with multi-component fits of the *in situ* EXAFS spectra collected at 400 °C after He-activation, to independently validate the employed reconstruction method and access detailed structural information on the preferred Cu local coordination environment associated with *1Al* and *2Al* sites. EXAFS fits substantially confirm the Cu-speciation evaluated from MCR-ALS analysis of temperature-dependent *in situ* XANES, but evidence that self-reduction is accompanied by higher levels of structural disorder in the Cu local environment. The composition-driven reducibility trends and the nature of the ZCu(I) structural component are further investigated using FTIR spectroscopy. Low-temperature IR spectra of N_2 adsorbed on *vacuum*-activated Cu-CHA catalysts with different composition clearly show two components at 2292 cm^{-1} and at 2300 cm^{-1}, that we rationalize in term of the different cation local environment for *1Al* ZCu(I) sites in *8r* and *6r*, respectively.

All these findings synergically demonstrate that reducibility in Cu-CHA results from the balance between two distinct Cu-speciation-related effects: (i) at low Si/Al values (e.g. Si/Al = 5), redox-inert *2Al* sites in *6r* are favoured; (ii) at high Si/Al values (e.g. Si/Al = 29), redox-active *1Al* sites largely dominate, but the self-reduction of the correspondent Z[Cu(II)OH] complexes is hindered due to the low interaction probability among proximal acid sites, yielding a counterintuitive enhancement of the relative Cu(II) fraction in the He-activated state.

Finally, this study addresses the *grand* challenge of characterization in heterogeneous catalysis, demonstrating the potential of chemometric techniques, such as MCR-ALS, in the modelling of complex spectroscopic dataset, enabling an unprecedented level of understanding in a complex multi-component system.

Acknowledgements

EB acknowledges Innovation Fund Denmark (Industrial postdoc n. 5190-00018B). CL, KAL, IAP acknowledge the Mega-grant of the Russian Federation Government to support scientific research at the Southern Federal University, No. 14.Y26.31.0001. We thank P.N.R. Vennestrøm and S. Teketel (Haldor Topsøe A/S) for samples' synthesis, C. Tyrsted (Haldor Topsøe A/S) for support during XAS data collection, Fernando Chávez-Riva (Escuela Superior de Física y Matemáticas, Instituto Politécnico Nacional, Mexico) for support during FTIR measurements. We are grateful to M. Monte Caballero (ESRF) for his competent support during the ESRF beamtime on BM23. We are also indebted to M. Vincenti and E. Alladio (University of Turin) for fruitful discussion on MCR-ALS analysis and to D. K. Pappas (University of Oslo) for insightful discussion on the direct methane conversion over Cu-zeolites.

Notes and references

§This is clearly observed for Si/Al = 5 catalysts, where *2Al* $Z_2Cu(II)$ sites are present in large abundance (> 40% total Cu). In some of the other samples, where *2Al* $Z_2Cu(II)$ sites represent a minor component (< 20% total Cu), their concentration for temperatures higher than 250 °C is subjected to fluctuations in the ±5% total Cu range, which reliability is difficultly assessable. Interestingly, such fluctuations in the *2Al* $Z_2Cu(II)$ population occur concomitantly to the rise in reduced *1Al* ZCu(I) species and seem to correlate with a small transient increase in the concentration of hydrated Cu-complexes.

1. A. M. Beale, F. Gao, I. Lezcano-Gonzalez, C. H. F. Peden and J. Szanyi, *Chem. Soc. Rev.*, 2015, **44**, 7371-7405.
2. U. Deka, I. Lezcano-Gonzalez, B. M. Weckhuysen and A. M. Beale, *ACS Catal.*, 2013, **3**, 413-427.
3. T. V. W. Janssens, H. Falsig, L. F. Lundegaard, P. N. R. Vennestrøm, S. B. Rasmussen, P. G. Moses, F. Giordanino, E. Borfecchia, K. A. Lomachenko, C. Lamberti, S. Bordiga, A. Godiksen, S. Mossin and P. Beato, *ACS Catal.*, 2015, **5**, 2832-2845.
4. K. Narsimhan, K. Iyoki, K. Dinh and Y. Roman-Leshkov, *ACS Central Sci.*, 2016, **2**, 424-429.
5. A. R. Kulkarni, Z. J. Zhao, S. Siahrostami, J. K. Norskov and F. Studt, *ACS Catal.*, 2016, **6**, 6531-6536.
6. M. J. Wulfers, S. Teketel, B. Ipek and R. F. Lobo, *Chem. Commun.*, 2015, **51**, 4447-4450.
7. P. Tomkins, M. Ranocchiari and J. A. van Bolchoven, *Accounts Chem. Res.*, 2017, **50**, 418-425.
8. V. L. Sushkevich, D. Palagin, M. Ranocchiari and J. A. van Bokhoven, *Science*, 2017, **356**, 523-527.
9. M. Ravi, M. Ranocchiari and J. A. van Bokhoven, in press, doi:10.1002/anie.201702550.
10. J. J. Pluth, J. V. Smith and W. J. Mortier, *Mat. Res. Bull.*, 1977, **12**, 1001-1007.
11. C. Andersen, M. Bremholm, P. Vennestrøm, A. Blichfeld, L. Lundegaard and I. B., *IUCrJ*, 2014, **1**, doi:10.1107/S2052252514020181.
12. R. Q. Zhang, J. S. McEwen, M. Kollar, F. Gao, Y. L. Wang, J. Szanyi and C. H. F. Peden, *ACS Catal.*, 2014, **4**, 4093-4105.
13. D. W. Fickel, J. M. Fedeyko and R. F. Lobo, *J. Phys. Chem. C*, 2010, **114**, 1633-1640.
14. S. T. Korhonen, D. W. Fickel, R. F. Lobo, B. M. Weckhuysen and A. M. Beale, *Chem. Commun.*, 2011, **47**, 800-802.
15. U. Deka, A. Juhin, E. A. Eilertsen, H. Emerich, M. A. Green, S. T. Korhonen, B. M. Weckhuysen and A. M. Beale, *J. Phys. Chem. C*, 2012, **116**, 4809-4818.
16. U. Deka, I. Lezcano-Gonzalez, S. J. Warrender, A. L. Picone, P. A. Wright, B. M. Weckhuysen and A. M. Beale, *Micr. Mesop. Mater.*, 2013, **166**, 144-152.
17. S. Brandenberger, O. Krocher, A. Tissler and R. Althoff, *Catal. Rev.*, 2008, **50**, 492-531.
18. F. Gao, N. M. Washton, Y. L. Wang, M. Kollar, J. Szanyi and C. H. F. Peden, *J. Catal.*, 2015, **331**, 25-38.
19. F. Giordanino, E. Borfecchia, K. A. Lomachenko, A. Lazzarini, G. Agostini, E. Gallo, A. V. Soldatov, P. Beato, S. Bordiga and C. Lamberti, *J. Phys. Chem. Lett.*, 2014, **5**, 1552-1559.
20. I. Lezcano-Gonzalez, U. Deka, B. Arstad, A. Van Yperen-De Deyne, K. Hemelsoet, M. Waroquier, V. Van Speybroeck, B. M. Weckhuysen and A. M. Beale, *Phys. Chem. Chem. Phys.*, 2014, **16**, 1639-1650.
21. C. Paolucci, A. A. Parekh, I. Khurana, J. R. Di Iorio, H. Li, J. D. Albarracin Caballero, A. J. Shih, T. Anggara, W. N. Delgass, J. T. Miller, F. H. Ribeiro, R. Gounder and W. F. Schneider, *J. Am. Chem. Soc.*, 2016, **138**, 6028-6048.
22. K. A. Lomachenko, E. Borfecchia, C. Negri, G. Berlier, C. Lamberti, P. Beato, H. Falsig and S. Bordiga, *J. Am. Chem. Soc.*, 2016, **138**, 12025-12028.
23. F. Gao, D. Mei, Y. Wang, J. Szanyi and C. H. F. Peden, *J. Am. Chem. Soc.*, 2017, **139**, 4935–4942.
24. E. Borfecchia, K. A. Lomachenko, F. Giordanino, H. Falsig, P. Beato, A. V. Soldatov, S. Bordiga and C. Lamberti, *Chem. Sci.*, 2015, **6**, 548-563.
25. C. Tyrsted, E. Borfecchia, G. Berlier, K. A. Lomachenko, C. Lamberti, S. Bordiga, P. N. R. Vennestrom, T. V. W. Janssens, H. Falsig, P. Beato and A. Puig-Molina, *Catal. Sci. Technol.*, 2016, **6**, 8314-8324.
26. J. H. Kwak, H. Y. Zhu, J. H. Lee, C. H. F. Peden and J. Szanyi, *Chem. Comm.*, 2012, **48**, 4758-4760.
27. F. Gao, E. D. Walter, E. M. Karp, J. Luo, R. G. Tonkyn, J. H. Kwak, J. Szanyi and C. H. F. Peden, *J. Catal.*, 2013, **300**, 20-29.
28. A. Godiksen, F. N. Stappen, P. N. R. Vennestrom, F. Giordanino, S. B. Rasmussen, L. F. Lundegaard and S. Mossin, *J. Phys. Chem. C*, 2014, **118**, 23126-23138.
29. F. X. Llabrés i Xamena, P. Fisicaro, G. Berlier, A. Zecchina, G. T. Palomino, C. Prestipino, S. Bordiga, E. Giamello and C. Lamberti, *J. Phys. Chem. B*, 2003, **107**, 7036-7044.
30. S. C. Larsen, A. Aylor, A. T. Bell and J. A. Reimer, *J. Phys. Chem.*, 1994, **98**, 11533-11540.
31. G. T. Palomino, P. Fisicaro, S. Bordiga, A. Zecchina, E. Giamello and C. Lamberti, *J. Phys. Chem. B*, 2000, **104**, 4064-4073.
32. E. M. C. Alayon, M. Nachtegaal, A. Bodi, M. Ranocchiari and J. A. van Bokhoven, *Phys. Chem. Chem. Phys.*, 2015, **17**, 7681-7693.
33. K. A. Lomachenko, E. Borfecchia, S. Bordiga, A. V. Soldatov, P. Beato and C. Lamberti, *J. Phys.: Conf. Ser.*, 2016, **712**, 012041.
34. S. Bordiga, E. Groppo, G. Agostini, J. A. van Bokhoven and C. Lamberti, *Chem. Rev.*, 2013, **113**, 1736-1850.
35. L. Mino, G. Agostini, E. Borfecchia, D. Gianolio, A. Piovano, E. Gallo and C. Lamberti, *J. Phys. D-Appl. Phys.*, 2013, **46**, 423001.
36. C. Garino, E. Borfecchia, R. Gobetto, L. Salassa, J. A. van Bokhoven and C. Lamberti, *Coord. Chem. Rev.*, 2014, **277–278** 130-186.
37. J. A. van Bokhoven and C. Lamberti, eds., *X-Ray Absorption and X-ray Emission Spectroscopy: Theory and Application*, John Wiley & Sons, Chichester (UK), 2016.
38. C. Lamberti, S. Bordiga, M. Salvalaggio, G. Spoto, A. Zecchina, F. Geobaldo, G. Vlaic and M. Bellatreccia, *J. Phys. Chem. B*, 1997, **101**, 344-360.
39. M. H. Groothaert, J. A. van Bokhoven, A. A. Battiston, B. M. Weckhuysen and R. A. Schoonheydt, *J. Am. Chem. Soc.*, 2003, **125**, 7629-7640.
40. E. M. C. Alayon, M. Nachtegaal, A. Bodi and J. A. van Bokhoven, *ACS Catal.*, 2014, **4**, 16-22.
41. E. M. Alayon, M. Nachtegaal, M. Ranocchiari and J. A. van Bokhoven, *Chem. Comm.*, 2012, **48**, 404-406.
42. G. T. Palomino, S. Bordiga, A. Zecchina, G. L. Marra and C. Lamberti, *J. Phys. Chem. B*, 2000, **104**, 8641-8651.
43. J. S. McEwen, T. Anggara, W. F. Schneider, V. F. Kispersky, J. T. Miller, W. N. Delgass and F. H. Ribeiro, *Catal. Today*, 2012, **184**, 129-144.
44. P. N. R. Vennestrøm, T. V. W. Janssens, A. Kustov, M. Grill, A. Puig-Molina, L. F. Lundegaard, R. R. Tiruvalam, P. Concepción and A. Corma, *J. Catal.*, 2014, **309**, 477-490.
45. T. Gunter, H. W. P. Carvalho, D. E. Doronkin, T. Sheppard, P. Glatzel, A. J. Atkins, J. Rudolph, C. R. Jacob, M. Casapu and J. D. Grunwaldt, *Chem. Commun.*, 2015, **51**, 9227-9230.
46. L. S. Kau, D. J. Spirasolomon, J. E. Pennerhahn, K. O. Hodgson and E. I. Solomon, *J. Am. Chem. Soc.*, 1987, **109**, 6433-6442.
47. M. Sano, S. Komorita and H. Yamatera, *Inorg. Chem.*, 1992, **31**, 459-463.

48. E. I. Solomon, D. E. Heppner, E. M. Johnston, J. W. Ginsbach, J. Cirera, M. Qayyum, M. T. Kieber-Emmons, C. H. Kjaergaard, R. G. Hadt and L. Tian, *Chem. Rev.*, 2014, **114**, 3659-3853.
49. P. S. Salmon, G. W. Neilson and J. E. Enderby, *J. Phys. C.*, 1988, **21**, 1335-1349.
50. M. Benfatto, P. D'Angelo, S. Della Longa and N. V. Pavel, *Phys. Rev. B*, 2002, **65**, 174205.
51. P. Frank, M. Benfatto, R. K. Szilagyi, P. D'Angelo, S. Della Longa and K. O. Hodgson, *Inorg. Chem.*, 2005, **44**, 1922-1933.
52. J. Chaboy, A. Munoz-Paez, P. J. Merkling and E. S. Marcos, *J. Chem. Phys.*, 2006, **124**, 064509.
53. K. Kervinen, P. C. A. Bruijnincx, A. M. Beale, J. G. Mesu, G. van Koten, R. Gebbink and B. M. Weckhuysen, *J. Am. Chem. Soc.*, 2006, **128**, 3208-3217.
54. J. M. Tranquada, S. M. Heald and A. R. Moodenbaugh, *Phys. Rev. B*, 1987, **36**, 5263-5274.
55. C. Prestipino, G. Berlier, F. Xamena, G. Spoto, S. Bordiga, A. Zecchina, G. T. Palomino, T. Yamamoto and C. Lamberti, *Chem. Phys. Lett.*, 2002, **363**, 389-396.
56. M. H. Groothaert, K. Lievens, H. Leeman, B. M. Weckhuysen and R. A. Schoonheydt, *J. Catal.*, 2003, **220**, 500-512.
57. C. Lamberti, C. Prestipino, F. Bonino, L. Capello, S. Bordiga, G. Spoto, A. Zecchina, S. D. Moreno, B. Cremaschi, M. Garilli, A. Marsella, D. Carmello, S. Vidotto and G. Leofanti, *Angew. Chem.-Int. Edit.*, 2002, **41**, 2341-2344.
58. E. R. Malinowski, *Factor analysis in chemistry*, John Wiley & Sons, New York, 2002.
59. R. Tauler, *Chemometrics Intell. Lab. Syst.*, 1995, **30**, 133-146.
60. A. de Juan, J. Jaumot and R. A. Tauler, *Anal. Methods*, 2014, **6**, 4964-4976.
61. H. W. P. Carvalho, S. H. Pulcinelli, C. V. Santilli, F. Leroux, F. Meneau and V. Briois, *Chem. Mat.*, 2013, **25**, 2855-2867.
62. A. Voronov, A. Urakawa, W. van Beek, N. E. Tsakoumis, H. Emerich and M. Ronning, *Anal. Chim. Acta*, 2014, **840**, 20-27.
63. W. H. Cassinelli, L. Martins, A. R. Passos, S. H. Pulcinelli, C. V. Santilli, A. Rochet and V. Briois, *Catal. Today*, 2014, **229**, 114-122.
64. J. P. Hong, E. Marceau, A. Y. Khodakov, L. Gaberova, A. Griboval-Constant, J. S. Girardon, C. La Fontaine and V. Briois, *ACS Catal.*, 2015, **5**, 1273-1282.
65. A. Rochet, B. Baubet, V. Moizan, C. Pichon and V. Briois, *C. R. Chim.*, 2016, **19**, 1337-1351.
66. J. Jaumot, R. Gargallo, A. de Juan and R. Tauler, *Chemometrics Intell. Lab. Syst.*, 2005, **76**, 101-110.
67. P. D'Angelo, O. M. Roscioni, G. Chillemi, S. Della Longa and M. Benfatto, *J. Am. Chem. Soc.*, 2006, **128**, 1853-1858.
68. P. D'Angelo, A. Zitolo, V. Migliorati, G. Mancini, I. Persson and G. Chillemi, *Inorg. Chem.*, 2009, **48**, 10239-10248.
69. S. A. Bates, A. A. Verma, C. Paolucci, A. A. Parekh, T. Anggara, A. Yezerets, W. F. Schneider, J. T. Miller, W. N. Delgass and F. H. Ribeiro, *J. Catal.*, 2014, **312**, 87-97.
70. J. S. Woertink, P. J. Smeets, M. H. Groothaert, M. A. Vance, B. F. Sels, R. A. Schoonheydt and E. I. Solomon, *P. Natl. Acad. Sci. USA.*, 2009, **106**, 18908-18913.
71. H. J. Jang, W. K. Hall and J. dItri, *J. Phys. Chem.*, 1996, **100**, 9416-9420.
72. P. J. Smeets, R. G. Hadt, J. S. Woertink, P. Vanelderen, R. A. Schoonheydt, B. F. Sels and E. I. Solomon, *J. Am. Chem. Soc.*, 2010, **132**, 14736-14738.
73. E. A. Pidko, E. J. M. Hensen and R. A. van Santen, *Proc. R. Soc. A-Math. Phys. Eng. Sci.*, 2012, **468**, 2070-2086.
74. F. Göltl, P. Sautet and I. Hermans, *Catal. Today*, 2016, **267**, 41-46.
75. C. W. Andersen, E. Borfecchia, M. Bremholm, M. Jørgensen, P. Vennestrøm, C. Lamberti, L. Lundegaard and B. B. Iversen, in press, DOI: 10.1002/ange.201703808, doi: 10.1002/ange.201703808.
76. W. Loewenstein, *Am. Mineral.*, 1954, **39**, 92-96.
77. G. Busca, *Phys. Chem. Chem. Phys.*, 1999, **1**, 723-736.
78. S. Bordiga, C. Lamberti, F. Bonino, A. Travert and F. Thibault-Starzyk, *Chem. Soc. Rev.*, 2015, **44**, 7262-7341.
79. A. Vimont, F. Thibault-Starzyk and M. Daturi, *Chem. Soc. Rev.*, 2010, **39**, 4928-4950.
80. F. Giordanino, P. N. R. Vennestrom, L. F. Lundegaard, F. N. Stappen, S. L. Mossin, P. Beato, S. Bordiga and C. Lamberti, *Dalton Trans.*, 2013, **42**, 12741-12761.
81. J. Dědeček, B. Wichterlova and P. Kubat, *Micr. Mesop. Mater.*, 1999, **32**, 63-74.
82. F. Geobaldo, C. Lamberti, G. Ricchiardi, S. Bordiga, A. Zecchina, G. T. Palomino and C. O. Arean, *J. Phys. Chem.*, 1995, **99**, 11167-11177.

View Article Online
DOI: 10.1039/C7SC02266B

Table of Content Entry

Composition-driven Cu-speciation and reducibility in Cu-CHA zeolite catalysts: a multivariate XAS/FTIR approach to complexity

A. Martini, E. Borfecchia*, K. A. Lomachenko, I. Pankin, C. Negri, G. Berlier, P. Beato, H. Falsig, S. Bordiga, C. Lamberti.

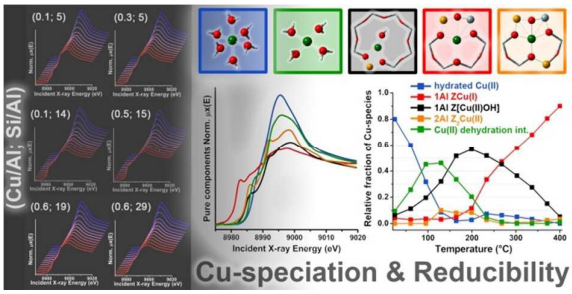

Multivariate XAS analysis and *in situ* FTIR enable an unprecedented quantitative understanding of the composition impact on temperature-dependent Cu-speciation and reducibility in Cu-CHA zeolite catalysts.